I
Ceramic Material Classes

Ceramics Science and Technology Volume 2: Properties. Edited by Ralf Riedel and I-Wei Chen

ISBN: 978-3-527-31156-9

1
Ceramic Oxides

Dušan Galusek and Katarína Ghillányová

1.1
Introduction

Ceramic oxides represent the most extensive group of ceramic materials produced today. Traditionally, but rather artificially, the oxide ceramics are divided into "traditional" and "advanced" groups. The "traditional" ceramics include mostly silica-based products prepared from natural raw materials (clays), including building parts (bricks, tiles), pottery, sanitary ware, and porcelain, but also ceramics with other main components (e.g., alumina, magnesia), which are applied in the field of electroceramics (insulators), or industrial refractories.

"Advanced" ceramics require a much higher quality and purity of raw materials, as well as the careful control of processing conditions and of the materials' microstructure. They usually comprise oxides, which do not quite fall within the traditional understanding of the term "silicate" materials and ceramics. Oxides found in these ceramics include mostly oxides of metals such as aluminum, zirconium, titanium, and rare earth elements. Originally investigated mainly as materials for structural applications (especially alumina and zirconia), ceramic materials (and not only oxides) partly failed to meet the expectations, mainly due to problems with reliability and high production costs. In recent years, therefore, a significant shift has been observed in pursuing and utilizing the functional properties of ceramic materials, especially chemical (high inertness), optical, electrical, and magnetic properties. Another area of research which has been pursued in recent years is the refinement of microstructure to the nanolevel. It is widely anticipated that such microstructure refinement will not only improve the known properties of ceramics, but will also bring new properties to already known materials. The attempts to prepare nanostructure materials bring new challenges: from the synthesis of suitable nanopowders, through their handling, the rheology of nanosuspensions, and health and safety issues, to the development of sintering techniques that allow densification without any significant coarsening of the microstructure.

In the following sections, an attempt is made to address the questions of recent developments in the field of ceramic oxides. As this topic cannot be covered fully within the space available, oxides have been selected which are considered to be the

Ceramics Science and Technology Volume 2: Properties. Edited by Ralf Riedel and I-Wei Chen

ISBN: 978-3-527-31156-9

most important for the field (Al_2O_3, ZrO_2), as well as those that have recently become a subject of interest for the ceramic community due to their interesting properties, such as TiO_2, ZnO, CeO_2, and Y_2O_3. Those materials which are only used as minor components of ceramic materials, or ternary compounds such as titanates or spinels, have been excluded at this stage.

1.2 Aluminum Oxide

From the point of view of the volume of production, polycrystalline alumina is the material most frequently used as ceramics for structural applications. However, in comparison with for example, silicon nitride, where the influence of various additives on microstructure and properties has been well characterized and understood, and despite several decades of lasting research effort, alumina remains a material with many unknown factors yet to be revealed. Alumina-based materials can be divided roughly into three groups:

- **Solid-state sintered aluminas:** Here, research is focused on a better understanding of sintering processes with the aim of preparing nanocrystalline materials with superior mechanical properties (e.g., hardness and wear resistance), and possibly also transparency to visible light. The prerequisite for the successful preparation of submicrometer aluminas with desired properties are sufficiently fine-grained and reactive nanopowders of high purity. Their synthesis and characterization has, therefore, been intensively pursued during the past years.
- **Liquid-phase sintered (LPS) aluminas:** Despite the fact that LPS aluminas represent a substantial part of industrially produced alumina-based materials, and despite a tremendous amount of research work, many unknowns remain. Although sintering additives have a profound influence on mechanical properties (especially on hardness, creep, and wear resistance, and to a certain extent also on bending strength and fracture toughness), there remains some confusion as to how individual additives or their combinations influence the microstructure and behavior of alumina-based materials. The sintering additives used include mostly silica, alkali oxides, the oxides of alkali earth metals, and combinations thereof. Doping with rare earth oxides is studied with the aim of understanding and enhancing the creep resistance of polycrystalline aluminas.
- **Alumina-based composites:** These comprise especially zirconia-toughened alumina (ZTA), and alumina-based nanocomposites with non-oxide second phases such as SiC or TiC. However, the latter two, in particular, are beyond the scope of this chapter.

1.2.1 Crystal Structure

The only thermodynamically stable crystallographic modification of alumina is α-Al_2O_3, or corundum. *Corundum* has a hexagonal crystal lattice with the cell

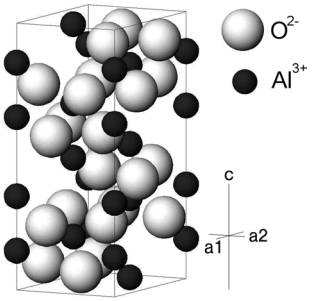

Figure 1.1 Crystal structure of α-Al_2O_3.

parameters a = 4.754 Å, and c = 12.99 Å. The ions O^{2-} are arranged in close hexagonal arrangement, with the cations Al^{3+} occupying two-thirds of the octahedral interstitial positions (Figure 1.1). Some selected materials properties of α-alumina single crystal are summarized in Table 1.1.

Except for the thermodynamically stable α modification, there exist also numerous metastable modifications, denoted γ, χ, η, ι, ε, δ, θ, and κ. These modifications are often used as supports for catalysts. All metastable modifications have a partially deformed closely packed hexagonal oxygen sublattice with various configurations of interstitial aluminum atoms. On approaching the equilibrium, the crystal lattice becomes more ordered until the stable α modification is formed. The type of metastable polymorph influences the morphology of the formed α-Al_2O_3 particles.

1.2.2
Natural Sources and Preparation of Powders

Aluminum is one of the most abundant elements on Earth and, in its oxidized form, is a constituent of most common minerals. Pure aluminum oxide is relatively rare, but may be found in the form of single crystal, when it is used as a gemstone in its colorless (sapphire) or red (ruby, due to the admixing of chromium) modifications.

Table 1.1 Some selected properties of single crystal α-alumina.

Property	Value	
Melting point	2053 °C	
Thermal conductivity	25 °C	40 W m K^{-1}
	1000 °C	10 W m K^{-1}
Thermal expansion coefficient (25–1000 °C)	Parallel with c	$8.8.10^{-6}$ K^{-1}
	Perpendicular to c	$7.9.10^{-6}$ K^{-1}
Density	3.98 g cm^{-3}	
Young's modulus	Parallel with c	435 GPa
	Perpendicular to c	386 GPa
Poisson ratio	0.27–0.30	

The most important raw material for the production of aluminum oxide is bauxite, which is a mixture of the minerals boehmite (α-AlO(OH)), diaspor (β-AlO(OH)), and gibbsite ($Al(OH)_3$), with a high content of various impurities such as Na_2O, SiO_2, TiO_2, and Fe_2O_3. Bauxite is refined using the Bayer process, which has been well described in many books dealing with the topic (e.g., Ref. [1]). Very pure commercial powders are prepared via the calcination of alum, $NH_4Al(SO_4)_2{\cdot}12\ H_2O$.

The preparation of submicrometer-grained aluminas requires well-defined pure nanopowders which, themselves, exhibit many exploitable characteristics, such as low-temperature sinterability, greater chemical reactivity, and enhanced plasticity. Thus, a range of methods has been developed for the preparation of nanopowders with desired properties. These can be roughly allocated to: (i) high-temperature/flame synthesis; (ii) chemical synthesis, including sol–gel; and (iii) mechanically assisted processes, such as high-energy milling.

1.2.2.1 High-Temperature/Flame/Laser Synthesis

The method usually comprises the injection of a suitable gaseous, or liquid aluminum-containing precursor into the source of intensive heat (e.g., laser [2], d.c. arc plasma [3–5], or acetylene, methane, or hydrogen flame [6, 7]), where the precursor decomposes and converts into the oxide. In most cases, transient aluminas are formed, and in order to obtain α-Al_2O_3 a further high-temperature treatment, usually accompanied by significant particle coarsening, is required. Possible precursors include metal–organic compounds such as trimethylaluminum or aluminum tri-*sec*-butoxide. Metastable alumina powders with particle sizes ranging from 5 to 70 nm can be prepared in this way.

1.2.2.2 Chemical Methods

These normally utilize the low- and medium-temperature decomposition of inorganic aluminum salts and hydroxides, or metal–organic compounds of aluminum. Typical precursors include aluminum nitrate and aluminum hydroxides. Hydrothermal conditions are often applied [8], but colloidal methods (sol–gel) have been extensively studied over the past three decades [9–11]. Recent efforts have been aimed at reducing the particle size of α-Al_2O_3, and decreasing the temperature of formation of α-Al_2O_3 from transient aluminas to $<1000\,^{\circ}C$ [12]. Results similar to those in sol–gel can be achieved with the use of metal ion–polymer-based precursor solutions. Here, the precursor solution (e.g., nitrate salt) is mixed with a water-soluble polymer, which provides a matrix for the dispersion of cations [13].

1.2.2.3 Mechanically Assisted Synthesis

These are based on the comminution of coarser-grained powders by high-energy milling or grinding. In this case, the minimum particle size is limited to approximately 40 nm [14], although further grinding may lead to severe aggregation and subsequent densification of the aggregates under mechanical stress. The high-energy ball-milling of γ-Al_2O_3 nanopowder with a small fraction of α-Al_2O_3 nanocrystalline seeds (both with an average particle size 50 nm) was reported to facilitate the transformation of milled powder to α-Al_2O_3 [15].

1.2.3
Solid-State Sintered Alumina

Strictly speaking, there are very few commercially available polycrystalline aluminas which could be defined as solid-state sintered. Even the materials prepared from ultrapure powders (purity >99.99%) develop a thin layer of intergranular amorphous film at the grain boundaries, as the result of the presence of trace impurities (e.g., Ca, Mg, Si, to mention the most important) which are always present in the starting powder [16]. Due to low lattice solubility of impurities in alumina, which usually do not exceed several ppm, the impurities segregate to the grain boundaries. Their concentration at interfaces increases as the grains grow during the course of densification, and the total area of interfaces (grain boundaries) per unit volume decreases. As soon as the preconcentration of the impurities exceeds a critical value, an amorphous grain boundary film is formed at the originally crystalline alumina–alumina interfaces. Hansen and Philips found that almost all the grain boundaries of a commercial 99.8% alumina were wetted by an amorphous film containing SiO_2 and CaO in addition to Al_2O_3 [17]. Harmer found that a commercial 99.98% alumina was sufficiently impure to contain a thin glassy film at the grain boundaries [18]. Processing (homogenization, pressing, the use of pressing additives, and sintering) represents another source of impurities. For example, the use of an electric furnace with $MoSi_2$ heating elements during sintering is known to contaminate the sintered materials with silicon, which is evaporated from the elements in the form of SiO, and then transported into the open porosity of the sintered body. Special precautions, such as the protection of specimens made from ultra-high-purity alumina (99.999%) in a closed sapphire tube, are then necessary to keep the grain boundaries clean [19]. The recently reported translucent or transparent aluminas with submicrometer microstructure represent one particular exception in this respect.

1.2.3.1 Submicrometer and Transparent Alumina

In submicrometer aluminas, the area of intergrain interfaces can be so high that the critical concentration of segregated impurities is not achieved and grain boundary glass is not formed. Submicrometer aluminas were reported to have increased hardness [20], a high mechanical strength [21–23], and a high wear resistance [24] in comparison with their coarser-grained counterparts, with possible application for cutting inserts [25].

Alumina is known to transmit infrared (IR) radiation and, if sintered to a high density (residual porosity <0.1%), it also transmits visible light. Possible applications then include high-pressure envelopes of sodium, or metal halide discharge lamps [26, 27], and impact layers of transparent armors with a high level of ballistic efficiency against armor-piercing ammunition (Figure 1.2). One potential use of alumina in the latter role has been already demonstrated with the use of sapphire single crystals in transparent armor systems [28].

At the present stage of knowledge, submicrometer-grained aluminas are in most cases only translucent or, at the best, are transparent with the linear transmission of

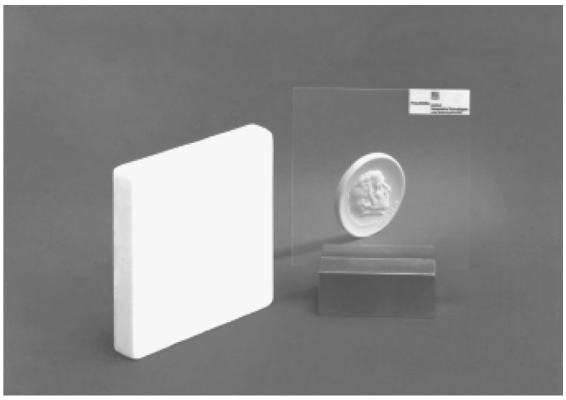

Figure 1.2 Comparison of an opaque tile (advanced ceramic armor, residual porosity 0.3%) and of a transparent window (residual porosity unmeasurable <0.03%) [35].

visible light at a level which is about 70% that of a sapphire single crystal of optical quality [29]. The visible light in polycrystalline alumina is scattered at grain boundaries as the result of alumina birefringence, and also due to light scattering at residual pores. It has been postulated that the linear transmission of visible light could be markedly increased by a further decrease in grain size to less than 340 nm – that is, below the wavelength of visible light [29], and by the complete elimination of any residual porosity (<0.1%). However, this goal is usually not attainable by normal sintering process, as the complete elimination of residual porosity requires long soaking times at high temperature, which is always accompanied by significant, and often abnormal, grain growth triggered by the presence of impurities and the formation of a grain boundary melt. The sintering trajectories of submicrometer alumina powders indicate that the majority of grain growth takes place above 90% relative density or, more specifically, at the very end of the sintering process when the last 3% of porosity is eliminated [30, 31]. As a result, a threefold or higher increase in grain size with respect to the original size of the alumina powder particles is observed. In order to solve this puzzle, special sintering techniques may be applied, such as microwave [32] or spark plasma sintering [33]; alternatively, pressure must be used, such as hot isostatic pressing (HIP) or sinter-HIP techniques [34], in order to prepare transparent polycrystalline alumina with a submicrometer grain size. Pressureless sintering to densities >99.9% at low temperatures (~1200 °C for minimum grain growth) is enabled by advanced processing approaches that yield green bodies with improved homogeneity and particle coordination [35].

1.2.4
Liquid-Phase Sintered (LPS) Aluminas

The glass present in alumina originates either from the materials' and processing impurities (Ca, Si, alkalis), or from substances added intentionally to influence

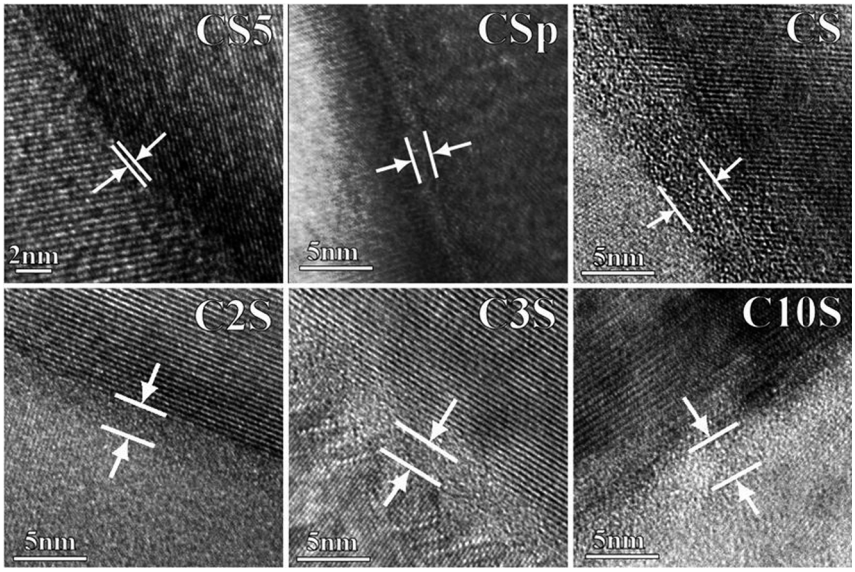

Figure 1.3 High-resolution transmission electron microscopy images of the grain boundaries of alumina samples sintered with 5 wt% calcium silicate additives. The numbers in the names of the specimens denote the molar ratio CaO/SiO_2 (e.g., CS5 = $CaO{\cdot}5\,SiO_2$). The change in grain boundary thickness with the composition of liquid forming additives is obvious [43].

sintering. Among these, the alumina–calcia–silica system is of considerable importance as it forms eutectics with melting temperatures in the range of 1200–1400 °C. The presence of SiO_2 and CaO results in the formation of a wetting aluminosilicate melt; sintering is then accelerated by dissolution–reprecipitation of the alumina particles in the melt. After cooling to room temperature, the melt solidifies to a glass, which forms several-nanometer-thick films at the intergrain faces. The equilibrium thickness of the film is defined by its chemical composition (Figure 1.3) [36, 37]. The co-doping of alumina with as little as 0.15 wt% CaO and 0.15 wt% SiO_2 ensures complete wetting of the grain boundaries with aluminosilicate glass [38]. The glass, which is "in excess" with respect to the formation of the film with equilibrium thickness, is accommodated in pockets at the grain boundary intersections, known as "triple pockets."

Both, silicon and calcium promote excessive growth along the basal planes of alumina crystals, known as abnormal grain growth (AGG), when present above critical concentrations that correspond roughly to their solubility limits [39]. As a result, platelike alumina grains grow. Abnormal platelike alumina grains are observed also in materials doped with $Na_2O + SiO_2$, $SrO + SiO_2$ and $BaO + SiO_2$ [40], TiO_2 [41], or SiO_2 and Y_2O_3 [42]. Although there is no general agreement on what is the driving force for AGG, it is usually attributed to the solubility anisotropy between growing and shrinking grains due to their curvature, and to the anisotropy of solid–liquid interfacial energies of various crystallographic faces of α-alumina

crystals, and hence the differential wetting of various crystallographic faces of alumina crystals. However, others have suggested that AGG is in fact the consequence of an uneven distribution of impurities and sintering aids [43, 44].

Molecular dynamics (MD) simulations of grain boundaries wetted with calcium silicate glass indicate that cagelike structures form at the interfaces between alumina grains and amorphous silicate film, which can accommodate metal cations such as calcium or magnesium [45]. Up to a concentration of 12 atom% calcium atoms are segregated in these cagelike structures, decreasing the glass/grain interfacial energy (Figure 1.4) [46, 47]. As the content of calcia grows beyond 12 atom%, this is increasingly accommodated in the glassy phase, disrupts siloxane bonding, and weakens grain boundaries. If the content of calcium in grain boundary glass exceeds 30 atom%, then an abnormal grain growth is triggered [47]. The MD simulations also suggest that the presence of Ca in intergranular film affects the behavior of the (0 0 0 1) basal plane, but not of the (1 1 $\bar{2}$ 0) prism plane of alumina crystals [48, 49]. This different adsorption behavior is caused by the formation of specific bonds between intergranular film species and surface species that limit further adsorption. These simulation results are indicative of the preferential growth that is consistent

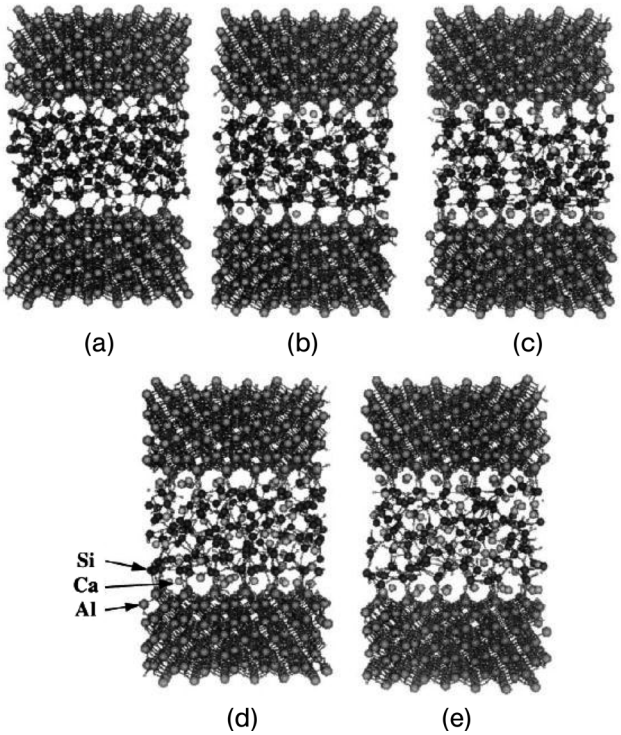

Figure 1.4 Examples of the final configurations of various compositions of the 600 atom calcium silicate intergranular films. The atom types are labeled in (d). As the number of Ca ions segregated to the interfaces increases, the interfaces become more ordered. (a) 0% CaO; (b) 12% CaO; (c) 22% CaO; (d) 32% CaO; (e) 41% CaO [64].

with the anisotropic growth of alumina crystals containing calcium aluminum silicate (CAS) intergranular films, as observed experimentally.

The addition of magnesium oxide is known to prevent the abnormal grain growth of alumina, both in very pure and liquid-phase-sintered materials. The microstructure then consists of equiaxed grains with narrow distribution of dihedral angles close to 120° [50]. There is no general agreement as to how MgO suppresses grain growth, but it is generally believed that the addition of MgO reduces the anisotropy of the solid–liquid interphase energies of alumina grains, changing the wetting of alumina with silicate liquids [50]. MgO also reduces alumina grain boundary mobility through solid solution pinning, thus protecting the material against abnormal grain growth arising from nonuniform liquid-phase distribution [51]. Most recent observations have indicated that MgO has a profound influence on the atomic structure of grain boundaries. Whilst the grain boundaries of an anorthite liquid containing aluminas are flat, atomically smooth and facetted, the addition of magnesia to an anorthite liquid results in curved, atomically rough grain boundaries [52]. Such a roughening effect is equivalent to a decrease in edge energy, so that the number of grains which can grow increases rapidly. As a consequence, many grains grow simultaneously and impinge upon each other such that AGG cannot occur [53].

Bae and Baik determined the minimum concentration of magnesia required to suppress the AGG in aluminas doped with ppm levels of silica and calcia [19]. The AGG does not take place if the amount of magnesia doping is approximately equal to the content of AGG-triggering impurities combined. Similar conclusions have been drawn from the investigation of commercial aluminas containing several vol% of glass. Typically, AGG is suppressed if the $MgO/(CaO + BaO + Na_2O + K_2O)$ ratio is >1 [54].

Partial crystallization often depletes the grain boundary glass of elements which are built into emerging crystalline phases. The structure, thermal expansion, and temperature dependence of viscosity of the grain boundary glass are then significantly altered. However, the crystallization of nanometer-thin glass grain boundary films is thermodynamically not favored, due to mechanical constraints from adjoining faces of alumina crystals [55]. Any volume change during crystallization gives rise to the strain energy which opposes the transformation, and under such circumstances crystallization will occur primarily in triple pockets. Consequently, a composition gradient will develop between the grain boundary and crystallized triple pocket. Phases such as anorthite, gehlenite, mullite, grossite, various spinels, and cordierite may crystallize in triple pockets [56, 57].

1.2.5
Properties of Polycrystalline Alumina

Polycrystalline alumina is especially praised for its great hardness, being the hardest of oxide ceramics. Although hardness ranges over a wide interval, and decreases with increasing content of the grain boundary glass, in ultrafine-grained solid-state sintered aluminas the hardness exceeds that of sapphire single crystal.

Table 1.2 Characteristic properties of various polycrystalline aluminas.

Property	Al_2O_3 [wt%]				
	86–94.5	**94.5–96.5**	**96.5–99**	**99–99.9**	**>99.9**
Density [g cm^{-3}]	3.4–3.7	3.7–3.9	3.73–3.8	3.89–3.96	3.97–3.99
RT hardness [GPa] HV 0.5	9.7–12	12–15.6	12.8–15	15–16	19.3
Young's modulus [GPa]	250–300	300	300–380	330–400	366–410
RT bending strength [MPa]	250–330	310–330	230–350	550	550–600

The other mechanical properties – especially fracture strength and fracture toughness – are usually inferior to those in other structural oxide ceramics such as zirconia. The presence of glass decreases the Young's modulus, and also the strength, hardness, and refractoriness of alumina ceramics. The typical properties of aluminas of various purities are listed in Table 1.2 [50].

Fracture strength varies over a broad range, and is often impaired by the thermal expansion mismatch of intergrain glass and alumina, and the extent of glass crystallization, due to volume changes and associated microcrack formation during the course of devitrification [58].

The presence of glass can either improve or impair fracture toughness, depending on its thermal expansion [59]. For example, if the thermal expansion of glass is higher than that of the matrix, the grain boundaries will be under tension whereas the grains will be in compression. Cracks may then propagate preferentially along the grain boundaries, potentially increasing the fracture toughness. In such a case the presence of platelike grains increases the fracture toughness by deviating the crack path and increasing the energy required for further propagation of the crack [60]. A glass with a lower thermal expansion will impose compressive stress into the grain boundaries, making them stronger and forcing the cracks to propagate intragranularly.

Direct evidence of grain boundary glass composition and crystallization on the magnitude and distribution of thermal residual stresses in calcium silicate sintered aluminas has been obtained recently [49]. Such studies have revealed the presence of residual fluctuating local stresses (i.e., very short-range stresses associated with dislocations, point defects, small inhomogeneities, etc.) between 420 and 460 MPa. This is an order of magnitude higher than the stresses in pure polycrystalline alumina that result from thermal expansion anisotropy of the alumina crystals along the *c* and *a* crystallographic axes (from 30 to 270 MPa, depending on grain size, and thermal history) [61–64].

The wear resistance of polycrystalline alumina is greater than that of sapphire single crystals, and increases with decreasing grain size [65–71]. The wear behavior of alumina cannot be simply related to its mechanical properties, such as hardness and fracture toughness [72, 73]. For pure alumina of mean grain size $<1\,\mu m$, the dominant wear mechanism is either plastic grooving or, in the presence of water, tribochemical wear, leading to polishing with very slow material removal rates. This is

sometimes attributed to the formation of a layer of hydrated alumina, which accommodates the interfacial shear stresses [74]. For coarser-grain-sized aluminas (1–50 μm) the main wear mechanism is that of microfracture and crack interlinking, leading to grain detachment and the development of rough surfaces [71].

Little is known of the corrosion of polycrystalline aluminas, but in general it is considered to be very low, and even negligible (which explains why such little interest has been expressed in the study of the mechanism involved). However, the results of the few studies to be conducted have suggested that the corrosion of polycrystalline alumina is controlled by the corrosion resistance of the grain boundary glass.

The electric properties of alumina make it adaptable for use in many applications, ranging from electronic substrates to spark plug insulators to magnetohydrodynamic power generators. Alumina is a low-loss dielectric material, the dielectric constant placing it well within the insulating range with a value of 8.8 at 1 MHz [75]. The dielectric properties of sapphire are anisotropic, and there is a 20% difference in permittivity between the a- and c-axis directions of the sapphire single crystal [76]. The alumina single crystal has one of the lowest loss tangents known, at about 0.001 [77]. The electric properties of polycrystalline aluminas are influenced by the presence of grain boundary impurities, especially of alkalis, iron, and titanium [75]. Improvements in the insulating properties and a decrease in the loss tangent can be achieved by reducing the porosity [78], increasing the purity [79], or by eliminating any impurities with valence that is different from Al^{3+}, mainly H^{+}, Fe^{2+}, Mg^{2+}, Ca^{2+}, Si^{4+}, and Ti^{4+} [80]. Nevertheless, the presence of certain contaminants, such as TiO_2, can be advantageous in some cases, most likely due to the better final microstructure of Al_2O_3 [81].

1.3
Magnesium Oxide

Magnesia has been used traditionally for the fabrication of basic refractories mainly used in steelmaking, gradually developing from inexpensive doloma refractories through highly resistant magnesia linings to MgO refractories containing graphite, which decreases the wetting of bricks by molten slags. Recently, considerable attention has been paid to the fabrication of fully dense fine-grained, defect-free MgO, on the basis of its expected excellent mechanical, thermal, and optical properties [82]. Fully dense MgO exhibits a high transparency to both IR and visible light, from 300 nm to 7 μm, and therefore might potentially be used as a substitute for sapphire IR windows and protectors for sensors. Magnesium oxide (electrical grade) is used in the electrical heating industry due to its high dielectric strength and relatively high thermal conductivity. In addition, the combination of electrical and refractory properties facilitates its use in high-temperature crucibles, thermocouple tubes, kiln furniture, and insulators. Due to its high-temperature stability, porous magnesia is also a suitable candidate for the support of combustion

Table 1.3 Physical properties for single-crystal MgO.

Property	Value
Density	$3.58\,g\,cm^{-3}$
Solubility	0.00 062 g in 100 g water
Thermal conductivity	$42\,W\,m^{-1}\,K^{-1}$ at 0 °C
Coefficient of thermal expansion	10.8×10^{-6}/K at 0 °C
Dielectric constant	9.65 at 1 MHz
Young's modulus	250 GPa
Shear modulus	155 GPa
Poisson's ratio	0.18

catalysts used in a high-temperature environment. Vanadium on a magnesium oxide support (V/MgO) is used as a selective catalyst for the oxidative dehydrogenation of alkanes.

1.3.1
Crystal Structure and Properties of Single-Crystal MgO

Magnesium oxide is a highly ionic crystal, with the Mg−O bonds having about 80% ionic character, and with a cubic face-centered crystal lattice (space group Fm3m). MgO has no polymorph transitions from room temperature to melting point at 3073 K. The physical properties of the MgO single crystal are listed in Table 1.3.

1.3.2
Natural Sources and Production

Magnesia (MgO) occurs in Nature largely as magnesite ($MgCO_3$) and dolomite (Mg, Ca)CO_3, and also rarely in oxide form as the mineral *periclase*. Magnesia refractories containing MgO can be obtained from high-purity magnesite ores simply by beneficiation and subsequent calcination at 500–700 °C. Sea water, brines, and deposits of MgO-rich salts represent other commercial sources of magnesia. Sea water contains about 1 kg of MgO per 500 l, in the form of magnesium chloride; the latter is reacted with an alkali source (commonly lime or slaked doloma) to form a precipitate of $Mg(OH)_2$ that is then washed, filter-pressed, dried, and calcined in large rotary kilns at 750–900 °C [50].

For the synthesis of high-purity, fine-grained MgO powders with excellent sinterability, as are required for the preparation of optical-grade magnesia, chemical techniques are used. The range of methods used includes the evaporative spray decomposition of a suitable precursor solution (e.g., magnesium acetate) [83], the thermal decomposition of $MgCl_2$ to MgO and HCl with subsequent washing, the reaction of $MgCl_2$ with citric acid in an excess of ammonia [84], and a vapor-phase oxidation process [85]. The sinterability of magnesia powders can be markedly improved by mechanical activation (e.g., high-energy milling).

1.3.3
Polycrystalline Magnesia

Due to the refractoriness of magnesia, either a high temperature or the application of pressure is usually required to attain a high density, although this generally leads to an undesirable microstructure coarsening and deterioration of the mechanical properties. Additives that lower the sintering temperature include $SiO_2 + B_2O_3$ [86], fluorides (LiF) [87], and V_2O_5. With the addition of approximately 0.5 cat%, the latter facilitates a complete densification by pressureless sintering at temperatures as low as 1250 °C. The final microstructure consists of 10 μm MgO grains with $Mg_3V_2O_8$ precipitates [88].

Translucent or transparent MgO is prepared from fine, active high-purity MgO powders with the use of pressure-assisted sintering techniques such as hot pressing (HP), HIP, or spark plasma sintering (SPS). Translucency is achieved under relatively moderate conditions (HIP 1100 °C/0.5 h, 99.7% theoretical density, average grain size 0.8 μm). Much higher temperatures are required to achieve full transparency (HIP 1500–1600 °C, relative density 99.9%, in-line transmission 65% of the MgO single crystal); however, the mechanical properties of the resultant material with a mean grain size of 132–199 μm are poor [89]. The hot pressing of a magnesia nanopowder (particle size 11 nm) at 790 °C and 150 MPa yields dense MgO ceramics with a relative density >99.5%, and with an average grain size of 73 nm [90]. SPS at temperatures between 700 and 825 °C and pressures of 100–150 MPa yields fully dense transparent nanocrystalline MgO with an average grain size of 52 nm, and with in-line transmissions of 40% and 60% of the MgO single crystal for the yellow and red light wavelengths, respectively [91].

It is generally believed that nanocrystalline MgO should possess superior mechanical properties, especially of strength and hardness, in comparison with its microcrystalline counterparts. If this hypothesis were true, it has never attracted any scientific evidence, and to the present authors' knowledge there is no information currently available on the mechanical properties of pure nanocrystalline MgO.

1.4
Zinc Oxide

Zinc oxide (ZnO) is perhaps best known as a good base for white pigments in paints, tableware, sanitary ware, tiles, and glasses. It also finds industrial use in the rubber industry, and as a component of opaque sunscreens. Recently, ZnO has attracted significant attention as a material for ultraviolet (UV) light-emitters, varistors, transparent high-power electronics, surface acoustic wave devices, piezoelectric transducers, and gas-sensors, and also as a window material for displays and solar cells. The quality and control of conductivity in bulk and epitaxial ZnO have raised interest in the use of this material for short-wavelength light emitters and transparent electronics [92, 93]. As a wide bandgap semiconductor ($E_g = 3.2$ eV), ZnO is a candidate host for solid-state blue to UV optoelectronics, including lasers. The applications include high-density data storage systems, solid-state lighting, secure communications, and biodetection. The most significant barrier to the

widespread use of ZnO-related materials in electronic and photonic applications is the difficulty in carrier doping, particularly in achieving p-type material.

1.4.1 Crystal Structure and Properties of Single-Crystal ZnO

ZnO normally has the hexagonal (wurtzite) crystal structure with lattice parameters $a = 3.25$ Å and $c = 5.12$ Å (space group $P6_3mc$). The Zn atoms are tetrahedrally coordinated to four O atoms, where the Zn d-electrons hybridize with the oxygen p-electrons. Layers occupied by zinc atoms alternate with layers occupied by oxygen atoms [94]. Whilst a bond between the Zn and O atoms exhibits covalent characteristic in the *c*-direction, it is mostly ionic in the *a*-direction [95]; consequently, ZnO single crystals have highly anisotropic properties.

ZnO nanocrystals may have different structures, depending on the method of preparation. For example, nanoparticles formed by the oxidation of zinc vapor have the zinc-blende structure when smaller than 20 nm, and form tetrapod-like crystals on further growth [96]. ZnO particles prepared via the flash evaporation method have a cubic crystal structure [97].

1.4.2 Natural Sources and Production

The most important zinc ore is zinc sulfide, found as the mineral *sphalerite*. The majority of ZnO is produced by the so-called "French process," which has been utilized since 1844. For this, metallic zinc is melted at 419.5 °C in a graphite crucible and vaporized above 907 °C. The zinc vapor then reacts with oxygen in the air to form zinc oxide, which normally consists of agglomerated zinc oxide particles with sizes ranging from 0.1 μm to a few microns, and a purity of up to 99.9%. A modification of the French process, known as the catalyst-free combust-oxidized mesh (CFCOM) process, yields acicular ZnO nanostructures (rods, wires, tripods, tetrapods, plates). The so-called "active zinc oxide" which is used to prepare advanced ceramics, is produced by dissolving a zinc ore in hydrochloric acid, followed by alkali precipitation. The precipitated zinc hydroxide is then removed by filtration, calcined, and micronized to obtain the powdered form [98]. More sophisticated methods include the thermal decomposition of zinc oxalate dihydrate [$Zn(C_2O_4)\cdot 2\,H_2O$] [99], the microwave irradiation of a $Zn(NO_3)_2$ solution neutralized at pH ~8–12 [100], the homogeneous precipitation of $Zn(SO_4)$ or $Zn(NO_3)_2$ by urea at 100 °C [101], the direct conversion of $Zn(NO_3)_2\cdot 6\,H_2O$-derived zinc hydroxide gel to crystalline product [102], or the combustion synthesis of zinc nitrate with glycine [103].

1.4.3 Properties

The physical properties of ZnO crystals depend heavily on the concentration of native defects caused by deviations from the stoichiometric composition. A review on this subject is available in Ref. [104].

Table 1.4 Basic physical properties of single-crystal ZnO.

Property	Value
Density	$5.606\,g\,cm^{-3}$
Stable phase at 300 K	Wurtzite
Melting point	1975 °C
Thermal conductivity	*a*: $0.6\,W\,m^{-1}\,K^{-1}$
	c: $1–1.2\,W\,m^{-1}\,K^{-1}$
Electrical conductivity	*a*: $3\,\Omega\,cm$
	c: $8.2\,\Omega\,cm$
Coefficient of linear thermal expansion	*a*: $6.5 \times 10^{-6}\,K^{-1}$
	c: $3.0 \times 10^{-6}\,K^{-1}$
Refractive index	*a*: 2.008
	c: 2.029
Energy gap	3.2 eV, direct

Although the basic physical characteristics of ZnO are summarized in Table 1.4, uncertainties persist with regards to some of these values. For example, the thermal conductivity exhibits a spread of values, most likely due to the presence of various crystal defects, such as dislocations [105].

Pure ZnO is an n-type semiconductor due to the incorporation of excess Zn, which causes a donor band conduction at low temperatures. A direct band gap of zinc oxide semiconductor is 3.2 eV (387 nm, deep violet/borderline UV). The bandgap can be altered by doping ZnO with divalent substitutes on the cation site: the addition of Cd reduces the bandgap to ~3.0 eV [106], while substitution of Zn by Mg increases the bandgap to ~4.0 eV.

The mechanical properties of polycrystalline ZnO ceramics are of special importance for their applications as varistors (see Section 1.4.4.1). When a varistor experiences a high-current pulse, the electrical energy is quickly converted to heat. The inertia of the material, which resists its thermal expansion, and the resonances of the resultant elastic waves in the block, may lead to microcracks and finally to mechanical failure [107]. Characteristic values of mechanical properties of ZnO ceramics are 1.2–1.4 MPa $m^{1/2}$ for fracture toughness, and 100–125 MPa for flexural strength.

1.4.4 Applications

1.4.4.1 ZnO-Based Varistors

Zinc oxide is best known for its use in varistors – that is, resistors with strongly nonlinear current–voltage characteristics. Such behavior was first reported in 1971 by Matsuoka, who observed the nonlinear electric properties of ZnO ceramics doped with Bi_2O_3, CoO, MnO, Cr_2O_3, and Sb_2O_3, and attributed such behavior to the presence of a bismuth-rich phase between the ZnO grains [108]. The nonlinear electrical characteristics of the nanometer-thick grain boundary phase is controlled by double Schottky barriers that result from electrons being trapped at the interface

and screened by the ionized shallow and deep bulk defects [109–112]. As a result, the conductivity of ZnO-based varistors increases by several orders of magnitude when a characteristic voltage is exceeded. This switching property of varistors, which is not only reversible but also very fast, provides an opportunity for their use as surge arresters in power transmission, and for the protection of electronic devices.

The current–voltage curve of a varistor consists of three distinct regions [113]:

- Pre-switch, where the behavior is ohmic and the resistance is controlled by the low grain-boundary conductivity.
- Switch or breakdown, where the behavior is nonlinear.
- High-current ohmic, where the resistance is controlled by the grain conductivity.

Various dopants may either alter or improve the nonlinear behavior of ZnO varistors, the most important being Bi_2O_3 and Sb_2O_3. Today, a wide range of additives is used in commercial varistors, and these usually comprise up to 10 components including Bi_2O_3, Sb_2O_3, Co_3O_4, SnO_2, Cr_2O_3, MnO/MnO_2, Al_2O_3, and Ag_2O. To assess the exact role of any of these is virtually impossible, as many of the dopants have a high vapor pressure at the temperature of sintering, such that the composition often changes due to component vaporization. Uncontrolled Bi_2O_3 vaporization is often a critical parameter in the manufacture of commercial varistors [114, 115].

Bi_2O_3 is vital for the successful sintering of zinc oxide-based ceramics, due to the formation of a low-temperature eutectic with ZnO at 740 °C. The solubility limit of bismuth III-oxide in ZnO may be up to 25 mol% [116]. The bismuth-containing melt cools to form an amorphous phase (located mainly in triple grain boundary junctions and to a lesser extent at the grain boundaries), and a secondary crystalline pyrochlore phase of nominal composition $Zn_2Bi_3Sb_3O_{14}$. The segregation of bismuth and oxygen (and to a certain extent also of other dopants) at the grain boundaries is crucial to achieve specific varistor properties.

Sb_2O_3 is added for better microstructure control during the course of sintering. At low temperatures, Sb_2O_3 binds Bi_2O_3 and forms the pyrochlore phase, thus shifting the onset of liquid-phase sintering to a higher temperature. The pyrochlore then reacts with ZnO to yield an electrically insulating grain boundary pinning spinel phase ($Zn_7Sb_2O_{12}$) [117] and free Bi_2O_3 [116, 118]:

$$2ZnO + 3/2\ Sb_2O_3 + 3/2\ Bi_2O_3 + 3/2\ O_2 \xrightarrow{T<900\ ^\circ C} Zn_2Bi_3Sb_3O_{14}\ (\text{pyrochlore}) \tag{1}$$

$$2Zn_2Bi_3Sb_3O_{14} + 17ZnO_3 \xrightarrow{900-1000\ ^\circ C} Zn_7Sb_2O_{12} + 3Bi_2O_3\ (\text{liquid}) \tag{2}$$

Both, spinel and pyrochlore accommodate excess dopants, the concentrations of which exceed their solubility limits in ZnO, and therefore they concentrate at grain boundaries [113]. The microstructure of a ZnO varistor will then comprise ZnO grains, a bismuth-rich phase, and spinel grains, which can be located either inter- or intragranularly (Figure 1.5).

An inhomogeneous microstructure results in the formation of preferred current paths in a varistor, its local overheating, and mechanical failure. Microstructural

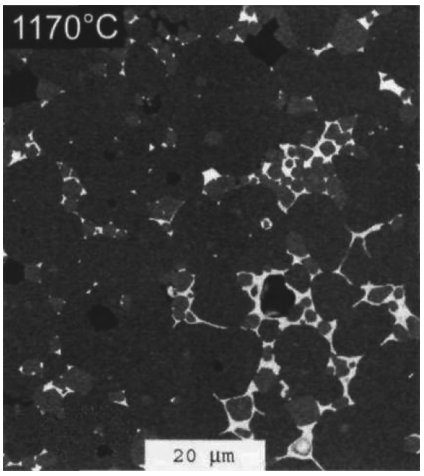

Figure 1.5 A backscattered-electron microscopy image of a polished ZnO varistor ceramics sintered at 1170 °C. The dark gray phase is ZnO, the light-gray is spinel, and the white is the bismuth-rich phase [131].

homogeneity is also important in order for a varistor to have a long service life; a continuous bismuth-rich network will contribute towards the leakage current that will provide the varistor with better pre-breakdown characteristics [119]. The leakage current in commercially formulated ZnO varistors is known to increase when Sb_2O_3 is replaced by SnO_2 [120].

The high volatility of Bi_2O_3 and the need for many minor additives in order to achieve a high performance, led to development of zinc oxide-based varistors with other varistor-forming oxides (VFOs). In Pr_6O_{11}-doped varistors, the most important two additives are Pr_6O_{11}, which gives rise to the nonlinear properties, and CoO, which enhances such properties [121–125]. Further improvement of the nonlinear properties by other minor additives (e.g., by Dy_2O_3) is not possible in the absence of cobalt oxide [126]. A simple three-oxide formulation, based on the addition of small amounts of vanadium and manganese oxides to zinc oxide, yields varistor behavior with a nonlinear coefficient in excess of 20 [127, 128]. Other VFOs which have been used include MnO_2 together with V_2O_5 [129], and a combination of NiO and CoO [130].

1.4.4.2 **Other Applications of ZnO Ceramics**

The majority of the ZnO that is produced is used in cosmetics, catalysis, and in the rubber industry, or as pigments in the production of tableware, sanitary ware, tiles, and glasses. The unique semiconducting properties of ZnO predestine its use in electronic devices. Notably, ZnO is interesting on the basis of its large exciton-binding energy (~60 meV), wide band gap and low lasing threshold. Consequently, ZnO one-dimensional semiconductor nanostructures (e.g., nanowires, nanorods or nanocolumns; see Figure 1.6) have become important fundamental building blocks for short-wavelength nanophotonic devices, and represent a substantial promise for integrated nanosystems [132]. Zinc oxide-based ceramics with nonlinear

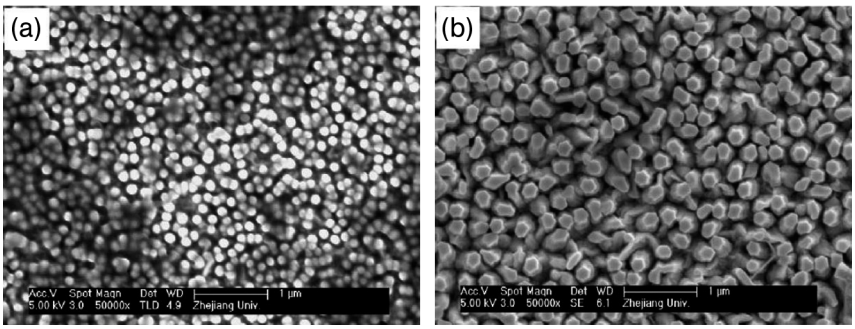

Figure 1.6 Representative field emission scanning electron microscopy images of ZnO nanocolumns grown at 400 °C on a Si (001) substrate. (a) Grown for 30 min; (b) Grown for 50 min [132].

voltage–current characteristics (VCC) are used in gas sensors for NO_2 and volatile organic compounds (VOC), such as benzene, toluene, and xylene. ZnO-based diluted magnetic semiconductors (DMS) are used in spintronics applications.

1.5 Titanium Dioxide

Titanium dioxide (TiO_2) is probably best known, and most widely used, as a brilliant white pigment and component of sunscreens. Recently, it has attracted increasing attention in the electronics industry due to its high dielectric and semi-conducting properties, photocatalytic activity, and good biocompatibility.

1.5.1 Crystal Structure and Properties of Single-Crystal TiO_2

Titanium oxide forms three polymorphs: rutile, brookite, and anatase [133]:

- *Rutile* is a tetragonal mineral usually of prismatic habit, often twinned. The unit cell of rutile (space group $P4_2/mnm$, $a = 4.5845$ Å; $c = 2.9533$ Å, density 4.274 g cm^{-3}) contains titanium atoms at the corners and in the center. Each titanium atom is surrounded by an approximate octahedron of oxygen atoms, and each oxygen atom is surrounded by an approximate equilateral triangle of titanium atoms (Figure 1.7a).
- *Anatase* is a tetragonal mineral of octahedral habit. The unit cell has a space group $I4_1/amd$, with the parameters $a = 3.7842$ Å, $c = 9.5146$ Å, and a density of 3.895 g cm^{-3} (Figure 1.7b).
- *Brookite* is an orthorhombic mineral with the unit cell parameters $a = 9.184$ Å, $b = 5.447$ Å, $c = 5.145$ Å, the space group *Pbca*, and a density of 4.123 g cm^{-3} (Figure 1.7c).

Anatase and brookite are metastable phases, and their exothermic and irreversible conversion to rutile at high temperatures has been widely investigated. Both,

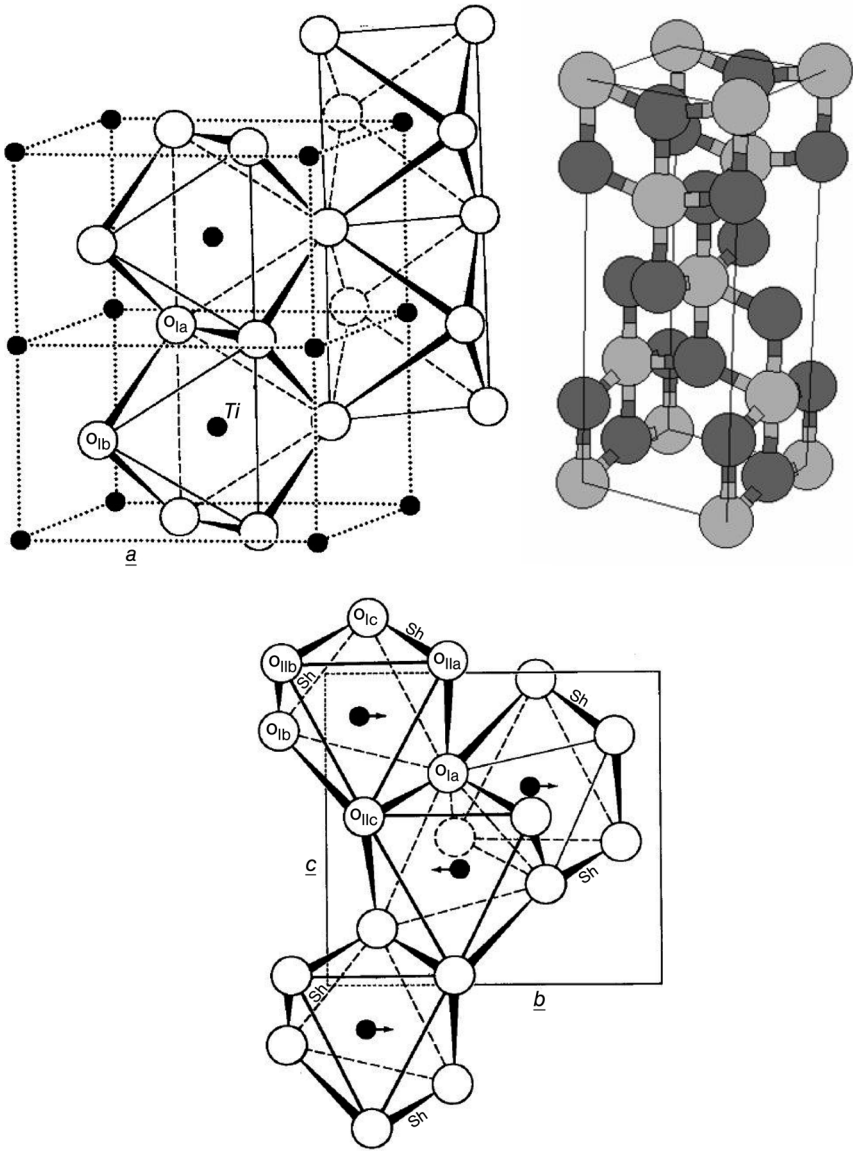

Figure 1.7 Crystal structures (from left to right) of rutile, anatase, and brookite [133].

ultrafine anatase and brookite transform upon coarsening to rutile when they reach a certain particle size [134, 135]. Once rutile has been formed, it grows much faster than anatase. The thermodynamic analysis of this phase stability indicates that anatase becomes more stable than rutile for particle sizes <14 nm. The transformation sequence and phase stability depend on the initial particle sizes of anatase and brookite [136–138].

1.5.2
Natural Sources and Production

The most important natural source of titania is iron titanate, known as the mineral *ilmenite*. Titanium oxide occurs also in its pure form, as the mineral rutile. Titanium dioxide is produced industrially via the sulfate process, whereby ilmenite ($FeTiO_3$) is hydrolyzed with sulfuric acid at >95 °C, after which TiO_2 is obtained by calcination at >800 °C. Rutile is purified by treatment with hydrochloric acid gas and conversion into titanium tetrachloride; TiO_2 is produced by treating the $TiCl_4$ with oxygen at >1000 °C.

The preparation of ultrafine-grained titania powders of specific phase composition has been described in several reports [139–141]; the starting materials and process conditions have a profound influence on the formation of TiO_2 nanocrystallites with a well-defined morphology (Figure 1.8.)

1.5.2.1 Synthesis of Anatase

Nanocrystalline anatase is usually prepared by hydrothermal synthesis or by sol–gel methods, using titanium alkoxides as the precursors. The TiO_2 precipitates can be produced by a reaction of $TiOCl_2$ and NH_4OH solutions, and subsequent treatment with NaOH or aging in boiling water [142]. A single-phase anatase powder is prepared by conventional or microwave hydrothermal (MH) synthesis from $TiOCl_2$ or a TiO_2 colloid [143, 144].

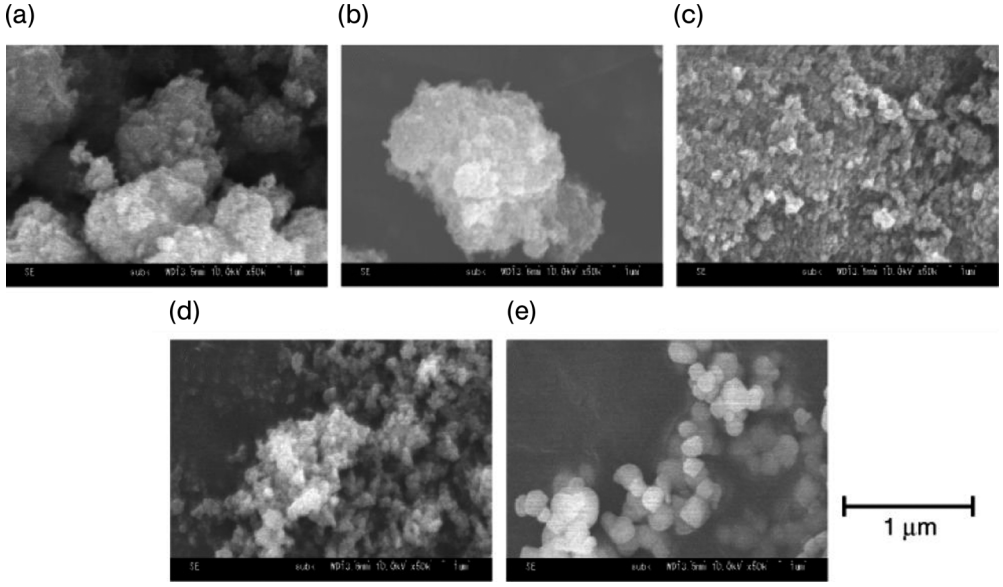

Figure 1.8 Morphologies of commercial anatase powders from various producers. (a) AMT-100; (b) AMT-600 (both Tayca Co., Osaka, Japan); (c) ST-01 (Ishihara Sangyo Kaisha Ltd., Osaka, Japan); (d) F-4 (Showa Denko K. K., Tokyo, Japan); (e) Sigma-Aldrich Co [147].

Anatase thin films are produced by dry processes such as sputtering and chemical vapor deposition (CVD), or by wet processes such as dip coating, sol–gel, spray-coating, and spin-coating. These methods require high temperatures (hundreds of °C) in order to achieve a fully crystalline anatase; the coating of surfaces with a lower thermal stability is therefore not possible. The development of procedures allowing near-ambient crystallization of anatase is therefore of profound importance. The available low-temperature syntheses utilize solutions of hazardous precursors, such as ammonium hexafluorotitanate [145], or titanium fluoride [146]. Crystalline anatase can be prepared under ambient conditions via the hydrolysis of tetraethylorthotitanate with acetylacetone, with added seeds of commercial anatase [147].

1.5.2.2 **Synthesis of Rutile**

The synthesis of pure rutile is difficult, as the crystallization normally yields mixtures of two, or even all three, polymorphs. Rutile is usually prepared via a hydrothermal synthesis from chlorides and oxychlorides of titanium seeded with rutile nanocrystals at temperatures below 250 °C. The addition of hydrochloric acid and aqueous alcohol solutions facilitates the preparation of rutile at temperatures between 40 and 90 °C [148]. Despite the risk of contamination, mineralizers (e.g., SnO_2, NH_4Cl or NaCl) are often used in order to reduce the size of rutile crystals. The reaction times of the hydrothermal synthesis of rutile can be significantly reduced by microwave irradiation [149]. A single-phase rutile with nanosized, well-dispersed particles prepared by a 2 h treatment of partially hydrolyzed 0.5 M $TiCl_4$ solution at 160 °C is shown in Figure 1.9.

1.5.2.3 **Synthesis of Brookite**

The synthesis of brookite is difficult since, as in the case of anatase, it normally yields a mixture of brookite and rutile and/or anatase. There is no general agreement as to

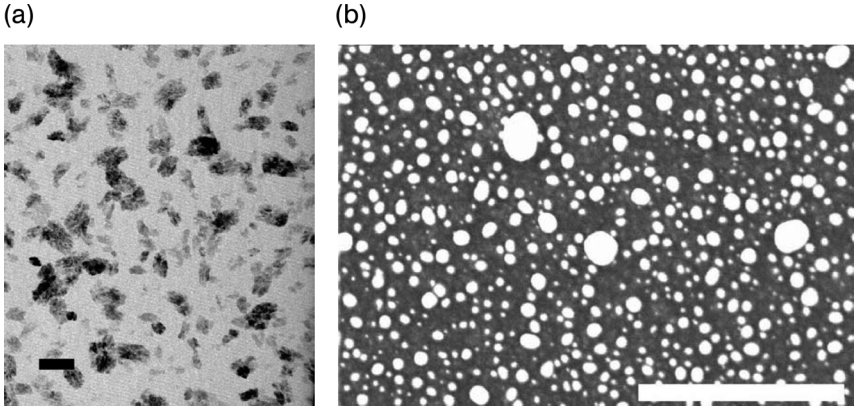

Figure 1.9 (a) Micrograph of rutile powder prepared by hydrothermal treatment of 0.5 M $TiOCl_2$ solution at 160 °C for 120 min (scale bar = 100 nm) [149]; (b) Micrograph of brookite nanoparticles with a mean size of ~30 nm, prepared by the method described in Ref. [152] (scale bar = 500 nm).

Table 1.5 Physical properties of various polymorphs of titania single crystals.

Property	Value		
	Anatase	**Rutile**	**Brookite**
Density [g cm^{-3}]	3.84	4.26	4.11
Melting point [°C]	—	1843	—
Refraction index	2.49	2.903	2.705 2.583
Electrical resistivity [Ω·cm, RT]	10^3–10^5		
Energy gap [eV]	3.23		

the factors responsible for the formation of brookite. Pottier *et al.* [150] have claimed that chloride ions are necessary in the reaction mixture to form brookite, whereas Kominami *et al.* [151] considered sodium salts, water and the organic titanium complex to be indispensable components for its successful synthesis. An example of 100% nanocrystalline brookite with an approximate particle size of 30 nm synthesized by the hydrolysis of $TiCl_4$ in acidic liquid media with isopropyl alcohol and water is shown in Figure 1.9b [152].

1.5.3
Properties of TiO_2 Polymorphs

Some physical properties of the three polymorphs of TiO_2 are listed in Table 1.5. Systematic data on titania single crystals are relatively scarce, and this applies especially to brookite, most likely due to difficulties with its preparation. The presence of impurities also results in a significant scatter of the property values.

1.5.4
Polycrystalline Titania

Polycrystalline TiO_2 is a functional ceramic of high technological importance that is used in the production of varistors, gas sensors, photovoltaic cells, dielectric resonators, and field-effect transistors as a gate dielectric. The electric properties of polycrystalline TiO_2 are heavily influenced by the presence of trace elements, impurities, as well as the oxygen partial pressure and temperature during the course of processing, all of which alter the bulk concentrations of the point and electronic defects. If sintering is allowed to occur in air or under a low oxygen partial pressure, a partial reduction of TiO_2 will take place. By using the Kröger–Vink notation, this reduction can be described in terms of the formation of oxygen vacancies [Eq. (3)], Ti^{4+} interstitials [Eq. (4)], Ti^{3+} interstitials [Eq. (5)], or oxygen vacancies and Ti^{3+} species in octahedral lattice sites [Eq. (6)] [153]:

$$2O_O^X \Leftrightarrow 2V_O^{\cdot\cdot} + 4e' + O_2 \tag{3}$$

$$Ti_{Ti}^{X} + 2O_{O}^{X} \Leftrightarrow Ti_{i}^{\bullet\bullet\bullet\bullet} + 4e' + O_2 \quad (4)$$

$$Ti_{Ti}^{X} + 2O_{O}^{X} \Leftrightarrow Ti_{i}^{\bullet\bullet\bullet} + 3e' + O_2 \quad (5)$$

$$2Ti_{Ti}^{X} + O_{O}^{X} \Leftrightarrow Ti'_{Ti} + V_{O}^{\bullet\bullet} + \frac{1}{2}O_2 \quad (6)$$

The powders used for the preparation of polycrystalline ceramics usually comprise rutile, or a mixture of rutile with other titania polymorphs. Both, brookite and anatase convert irreversibly to rutile in the temperature range of 700–920 °C; sintered materials will therefore usually comprise polycrystalline rutile. Sintering temperatures of up to 1500 °C are required to attain dense samples for powders with particle sizes of 0.2–3 μm, although lower sintering temperatures are possible with finer powders. Sintering aids such as $SrCO_3$, Bi_2O_3, and SiO_2 are used, which act either through increasing the concentration of lattice defects through the formation of a solid solution, or by forming a liquid phase at the temperature of sintering [154]. The physical properties of polycrystalline titania are summarized in Table 1.6.

1.5.5 Applications of TiO_2

Due to its very high refractive index, TiO_2 is a brilliant white pigment and opacifier that is used in paints, plastics, papers, foods, and any other applications which require a bright white color. Titanium dioxide is an important component of sunscreens, as the nanoparticles of rutile are transparent to visible light but reflect UV light. Due to its high dielectric constant, TiO_2 deposited in thin films is used in optical coatings for dielectric mirrors and beam splitters.

Table 1.6 Physical properties of fully dense sintered polycrystalline titanium dioxide ceramics.

Property		Value
Density		4.0–4.2 g cm^{-3}
Poisson's ratio		0.27
Compressive strength		680 MPa
Fracture toughness		2.8–6.1 MPa m$^{-1/2}$
Young's modulus		230 GPa
Microhardness [HV 0.5]		880
Electrical resistivity	(25 °C)	$10^{12}\,\Omega \cdot$ cm
	(700 °C)	$2.5 \times 10^{4}\,\Omega \cdot$ cm
Dielectric constant [1 MHz]		85
Dielectric loss tanδ [25 °C]		6×10^{-5}
Thermal expansion [RT–1000 °C]		9×10^{-6} K^{-1}
Thermal conductivity [25 °C]		11.7 W m K^{-1}

Titanium dioxide is an n-type semiconductor that is used in thin-film oxygen and humidity sensors [155, 156]. Doping with other metal oxides (e.g., iron oxides) increases the sensitivity and selectivity of the titania oxygen sensors [157, 158]. In comparison to zirconia, titania sensors have a better resistance against lead poisoning.

Titania is known to exhibit varistor properties, with a lower breakdown voltage than ZnO-based varistors. The first reported (Nb, Ba)-doped TiO_2 varistors had a nonlinear exponent of about 3–4 [159], but today Ta- and Ba-doped TiO_2-based varistors with a nonlinear coefficient in the range of 20–30 are well known [160]. Those dopants with a $+5$ valence, such as Nb and Ta, and with an ionic radius similar to that of Ti^{4+}, dissolve in the TiO_2 lattice and reduce its resistivity by donating conductive electrons [161]. Some codopants, such as Ba and Bi, tend to exsolve during cooling and react with rutile to form secondary phases, $Ba_2Ti_9O_{20}$ and $Bi_2Ti_4O_{11}$. Subsequent slow cooling decreases the Bi^{+3} (Bi'_{Ti}) acceptor concentration in rutile grains in near-grain boundary regions, thus reducing the barrier height with a corresponding reduction in nonlinear exponent values (Figure 1.10) [162].

Titanium dioxide, and anatase in particular, has strong photocatalytic properties under UV light, with both electron and hole pairs being generated in TiO_2. These respectively reduce and oxidize any substances adsorbed onto the anatase surface, thus producing the radicals OH^- and O^{2-} that are capable of decomposing most organic compounds and killing bacteria; consequently, this represents a major potential for anatase crystals to be used in water and air purification, or as wastewater remediation [163]. The reaction activity of anatase crystals is orientation-dependent; for example, water reduction and photooxidation each take place at more negative potentials for the anatase (0 0 1) surface than for the anatase (1 0 1) surface [164]. The orientation of anatase nanocrystals with (0 0 1) preferred growth would, therefore, be

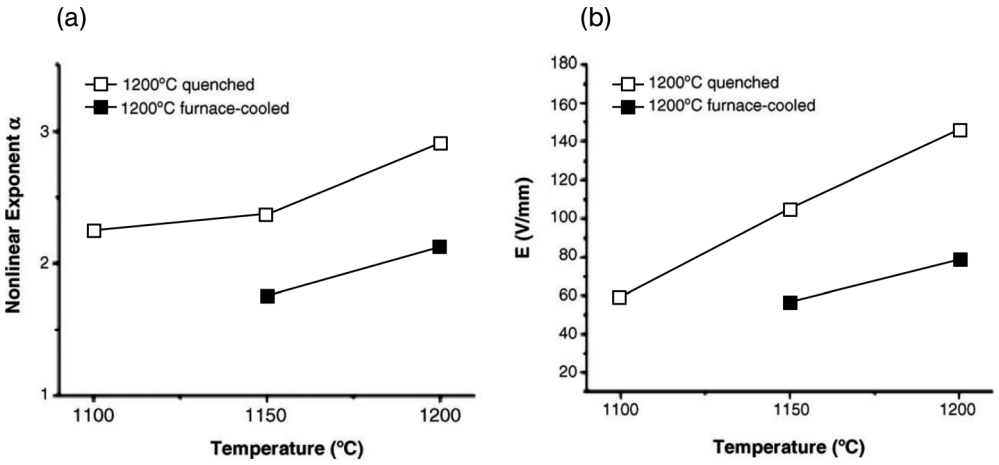

Figure 1.10 (a) The variation of nonlinear exponent and (b) breakdown voltage of Ba-doped titania varistors [162].

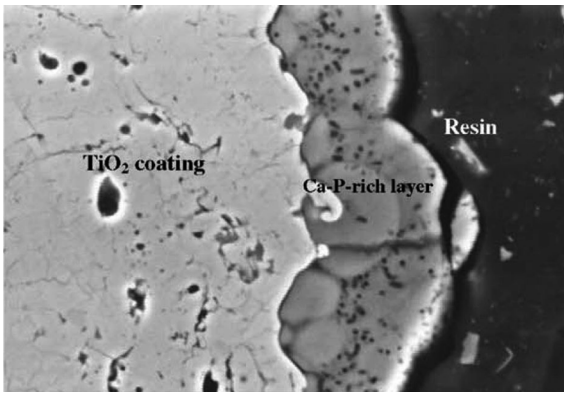

Figure 1.11 Cross-sectional view of hydroxyapatite layer formation on nano-TiO_2 coating after a four-week period soaking in a simulated body fluid [166].

expected to increase the charge conversion efficiency of photocatalysis. Anatase, when exposed to UV light, also becomes increasingly hydrophilic, providing a potential to produce windows with anti-fogging coatings or self-cleaning properties. Consequently, TiO_2 is added to paints, cements, windows, tiles, or other products in order to provide sterilizing, deodorizing, and anti-fouling properties. TiO_2 is also incorporated into outdoor building materials, where it will reduce the concentrations of airborne pollutants, such as VOC and NO_x.

A recently reported photocatalytic activity of brookite within the visible wavelength range also provides the opportunity for even broader applications of titania-based photocatalysts. For example, Showa Denko K.K. (Japan) have commercialized a new brookite nanoparticles-based photocatalyst that is responsive to visible light [165], although details of its synthesis are presently unavailable such that the company is the sole producer of brookite-based photocatalysts worldwide.

The biocompatibility of TiO_2 has been demonstrated by the formation of apatite on TiO_2 substrates in simulated body fluids [166–169] (Figure 1.11). As an example, plasma-sprayed TiO_2 coatings on Ti alloys have shown promising *in vivo* corrosion characteristics, and may act as a chemical barrier against the release of metal ions from medical implants [170].

1.6 Zirconium Oxide

Zirconia-based ceramics are characterized by a unique combination of high strength, toughness and chemical resistance, which allows their use in harsh environments under severe loading conditions. Typical applications include tools for cutting difficult materials such as Kevlar, magnetic tapes, plastic films, or paper items. It was shown long ago that wire-drawing dies and hot-extrusion dies made from zirconia could outperform their conventional counterparts [171]. Zirconia is considered as an

Table 1.7 Lattice parameters of zirconia polymorphs.

Crystal structure	Monoclinic	Tetragonal	Cubic
Space group	$P2_1/C$	$P4_2/nmc$	$Fm3m$
Unit cell parameters	$a = 5.156$ Å $b = 5.191$ Å $c = 5.304$ Å $\beta = 98.9°$	$a_t = 5.094$ Å $c_t = 5.177$ Å	$a_c = 5.124$ Å
Density [g cm^{-3}]	5.83	6.10 (calc.)	6.09 (calc.)

attractive matrix for nuclear applications, such as an inert matrix for the destruction of excess plutonium, or as a good host material for nuclear waste storage. Other applications include seals in valves, chemical and slurry pumps, thread guides, and bearings. Other important fields of application include biological implantation materials, examples being the replacement of worn or injured joints such as the hip or knee [172]. Functional applications of zirconia include (but are not limited to) thermal barrier coatings, solid electrolytes, oxygen sensors, and materials for fuel cells.

1.6.1
Crystal Structure and Properties of Single Crystals

Zirconia is known to exist as three, well-defined polymorphs, namely monoclinic, tetragonal, and cubic [173], although the existence of a high-pressure orthorhombic form has also been reported [174]. The lattice parameters of zirconia polymorphs are summarized in Table 1.7.

Monoclinic zirconia consists of a sevenfold coordinated Zr^{4+} cation, such that the oxygen ions with O_{11} coordination are almost tetrahedral, but with one angle in the structure differing significantly from the tetrahedral value (Figure 1.12a). Tetragonal

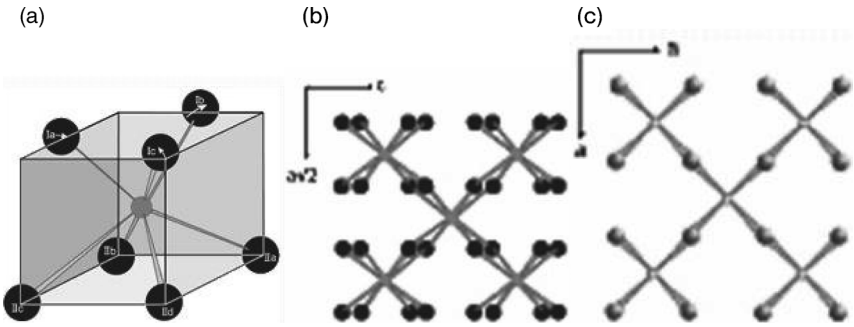

Figure 1.12 Crystal structures of (a) monoclinic, (b) tetragonal, and (c) high-temperature cubic ZrO_2 polymorphs.

Table 1.8 Some physical properties of single-crystal ZrO_2.

Property		Value
Transformation temperatures	m → t	950–1200 °C
	t → c	2370 °C
Melting point	Tetragonal	2677 °C
	Cubic	2500–2600 °C
Coefficient of thermal expansion		
Monoclinic	a	1.03×10^{-6}/K
	b	0.135×10^{-6}/K
	c	1.47×10^{-6}/K
Cubic		$7.05–13 \times 10^{-6}$/K (0–1000 °C)
Specific heat capacity [20 °C]		64.29 kJ mol^{-1} K^{-1}
Refractive index (cubic)		2.15–2.18
Young's modulus (tetragonal)		140–200 GPa
Hardness (cubic)		8–8.5 Mohs

zirconia contains the eightfold-coordinated Zr^{4+} cation with four oxygen ions placed at a distance of 2.065 Å in the form of a flattened tetrahedron, and four at 2.455 Å in an elongated tetrahedron rotated through 90 ° (Figure 1.12b). The high-temperature cubic polymorph has a face-centered CaF_2 structure with an eightfold-coordinated Zr^{4+} atom with oxygen ions arranged in two equal tetrahedra (Figure 1.12c).

Some physical properties of zirconia single crystals are summarized in Table 1.8. It should be noted, however, that these values are only for orientation; in the case of stabilized forms of the tetragonal and cubic polymorphs, the properties will be significantly influenced by the presence of stabilizing aids (see below).

1.6.2
Natural Sources and Production

Zirconia is found as the free oxide *baddeleyite*, always accompanied by hafnium oxide as the impurity; however, the most frequent source of zirconia is its compound oxide with silica, known as the mineral *zircon* ($ZrO_2 \cdot SiO_2$).

Pure zirconia is obtained via the chlorination and thermal decomposition of zirconia ores, their decomposition with alkali oxides, and lime fusion. The initial stage of the process is based on the chlorination of zircon in the presence of carbon at a temperature of 800–1200 °C in a shaft furnace:

$$ZrO_2 \cdot SiO_2 + C + 4Cl_2 \rightarrow ZrCl_4 + SiCl_4 + 4CO \quad (7)$$

On completion of the reaction the zirconium tetrachloride is distilled off, condensed, and then hydrolyzed with water to yield a solution of zirconium oxychloride, $ZrOCl_2$. The latter is then crystallized and the crystals calcined to produce hard granular ZrO_2.

The most common method for purifying zirconia ores is the breakdown of baddeleyite and zircon by reaction with sodium hydroxide at temperatures above 600 °C [175]:

$$ZrO_2 \cdot SiO_2 + 4NaOH \rightarrow Na_2ZrO_3 + Na_2SiO_3 + 2H_2O \quad (8)$$

Alternatively, sodium carbonate can be also used, at a temperature of approximately 1000 °C:

$$ZrO_2 \cdot SiO_2 + Na_2CO_3 \rightarrow Na_2ZrSiO_5 + CO_2 \quad (9)$$

$$ZrO_2 \cdot SiO_2 + 2Na_2CO_3 \rightarrow Na_2ZrO_3 + Na_2SiO_3 + CO_2 \quad (10)$$

The sodium silicate is removed by leaching in water, which at the same time hydrolyzes the zirconates to complex hydrated hydroxides of zirconia. These can be directly calcined to yield impure oxides, or further purified for example by treatment with sulfuric acid. The zirconyl sulfates formed are precipitated with a solution of ammonia to form the basic zirconium sulfate $Zr_5O_8(SO_4)_2 \cdot x\,H_2O$, and then calcined.

Lime fusion is based on the reaction of zircon with calcia, or doloma, which yields calcium zirconium silicate, calcium zirconate, calcium silicate, zirconium oxide, calcium magnesium silicate and the mixtures thereof, according to the reaction conditions:

$$CaO + ZrO_2 \cdot SiO_2 \xrightarrow{1000\,^\circ C} CaZrSiO_5 \quad (11)$$

$$2CaO + ZrO_2 \cdot SiO_2 \xrightarrow{1600\,^\circ C} ZrO_2 + CaSiO_4 \quad (12)$$

The calcium silicate is removed by leaching with hydrochloric acid, and the remaining zirconia washed and dried.

Recent research efforts have been focused on the synthesis of doped, stabilized zirconia powders, especially with nanometer-sized particles. Nanocrystalline stabilized powders are vital for the preparation of nanocrystalline materials, as their properties are fundamentally different from those of conventional powders, due to the extremely small crystalline dimension, superior phase homogeneity and low-temperature sinterability that significantly determines the later-stage processing and sintering properties of ceramics.

A large variety of methods which include (but are not limited to) hydrothermal or solvothermal synthesis, spray-drying, air-plasma-spraying, combustion synthesis (spray pyrolysis), autoignition, coprecipitation, and polymerization/sol–gel have been used for the preparation of stabilized zirconia nanopowders. Typical precursors comprise $ZrOCl_2 \cdot 8\,H_2O$, $ZrO(NO_3)_2 \cdot 6\,H_2O$, and nitrates, chlorides or other inorganic salts of stabilizing metals, such as Mg, Ca, Y, Ce, and Pr. The application of microwaves represents an efficient means of enhancing the crystallinity and decreasing the processing time of doped zirconia nanopowders. Ultrafine particles may be synthesized using complexing process, whereby the metal ions are retained in homogeneous solution with the aid of complexion agents such as lactic acid, citric

acid, or ethylenediaminetetra-acetic acid (EDTA). Precipitation of the particles occurs when the complex is broken and large amounts of nuclei are dumped into solution. At this point, almost all available energy is consumed in the formation of nuclei and, as a consequence, growth of the nuclei is limited such that ultrafine particles result from the process.

1.6.2.1 Phase Transformation of Zirconia

The phase transformation of zirconia is a process of major technological importance, notably the transformation from monoclinic (m) to tetragonal (t) zirconia that is associated with a volume decrease of approximately 3–5%. The transformation is generally described as a reversible, atermic, difusionless thermoelastic shear process, which proceeds at near-sonic velocities. However, recent investigations have suggested that the t $\rightarrow$ m transformation is a semi-thermoelastic rather than thermoelastic process, due to the presence of a large thermal hysteresis and a high critical driving force and reversible motion of the t–m interface, which can occur only under thermal stress [176].

A reverse t $\rightarrow$ m transformation and related volume increase during the course of cooling the zirconia parts from the processing temperature, which exceeds the reported temperature for unconstrained transformation of $1174 \pm 6\,^{\circ}\mathrm{C}$ [177], results in significant strains, which can be only accommodated by the formation of cracks. Thus, the fabrication of large parts of pure zirconia is not possible due to spontaneous failure on cooling.

Garvie *et al.* were the first to realize the potential for the phase transformation of zirconia in enhancing the mechanical properties of ceramics [178], and subsequently developed the concept of "transformation toughening." For this, the phase transformation of a metastable tetragonal zirconia particle can be induced by the stress field at the tip of a propagating crack. The volume change and shear strain associated with the transformation oppose the opening of the crack, thus increasing the resistance of the ceramic to crack propagation. One example of such a material is zirconia-toughened alumina (ZTA), in which the transformable tetragonal zirconia particles are embedded in a matrix with a high elastic modulus. This imposes elastic constraints that prevent transformation back to the monoclinic form. If a crack were to be extended under the stress, then large tensile stresses would be generated around the crack, especially ahead of the crack tip [179, 180]. These stresses would release the matrix constraints such that the transformable tetragonal inclusions would transform to monoclinic, and the resultant volume expansion ($\sim$3%) and shear strain ($\sim$1–7%) would lead to the generation of a compressive strain in the matrix. If this were to occur in the vicinity of the crack, then extra work would be required to move the crack farther.

There exists a size interval for zirconia particles, where the tetragonal particles can be transformed by stress. If the particles are less than critical size they will not transform, but if they are larger than the critical size then they will transform spontaneously. The spontaneous transformation of overcritical particles facilitates the additional toughening mechanism known as "microcracking." On cooling through the transformation temperature, the volume expansion of 3–5% is

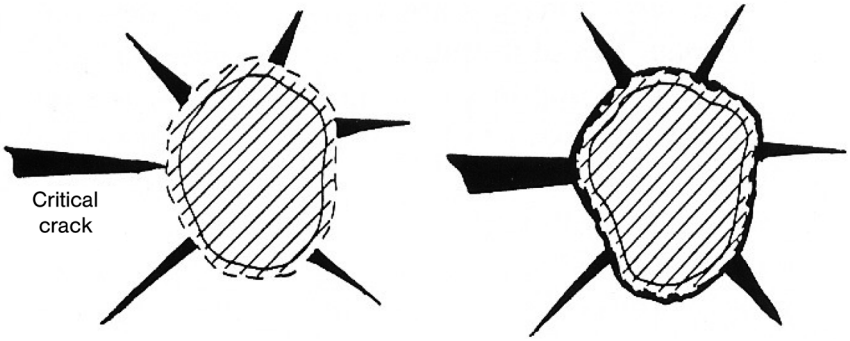

Figure 1.13 Microcrack formation around a transformed zirconia particle.

accommodated by the formation of radial microcracks around the zirconia particles. The fracture resistance is increased by the deviation of a propagating crack into the transformed particle, and bifurcation of the crack around it (Figure 1.13).

The critical size of transformable inclusions is significantly influenced by the presence of additives. If the content of stabilizing aids is sufficiently high, then the transformation can be suppressed entirely. This "stabilization" is in fact a kinetic stabilization of a solid solution in the cubic polymorph down to room temperature by alloying with an alkali earth oxide, or a rare earth oxide. A solid solution can be formed with any ion, provided that the ionic radius is within 40% of the ionic radius of Zr^{4+}. The term "full stabilization" refers to compositions which exhibit single-phase behavior over the whole range of temperatures from absolute zero to the melting temperature of zirconia. By avoiding the existence of a tetragonal phase at intermediate temperatures, the deleterious transformation back to a monoclinic polymorph is also avoided. Although the exact mechanism of stabilization is not clear, it has been suggested that alloying increases the ionic character of bonding, thus making the cubic structure more stable.

1.6.3
Partially Stabilized Zirconia

The addition of sufficient alloying component to facilitate a partial stabilization of the cubic phase leads to partially stabilized zirconia (PSZ), which exhibits an improved thermal shock resistance in comparison to fully stabilized zirconia, as well as an excellent fracture toughness. Today, four oxides – CaO, MgO, Y_2O_3, and CeO_2 – are commonly used to produce PSZ which, in fact, is a mixture of cubic and tetragonal/monoclinic phases that can be prepared by heat treatment of the cubic phase. This process is aimed at the development of a two-phase ceramic when the concentration of stabilizing agents is insufficient to produce full stabilization of the cubic structure.

1.6.3.1 **Mg-PSZ**

A typical Mg-PSZ contains approximately 8 mol% of MgO. The characteristic procedure when preparing Mg-PSZ involves sintering and heat treatment in the

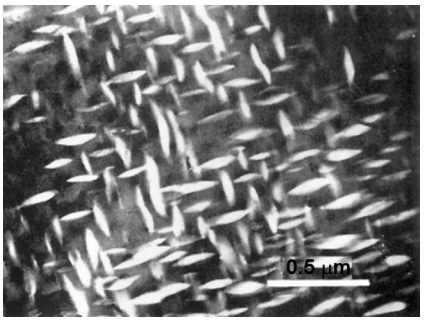

Figure 1.14 Oblate spheroids of tetragonal phase nucleated in a cubic ZrO_2 matrix.

cubic single-phase field (temperature $>1750\,^{\circ}C$), followed by a rapid cooling which does not allow the precipitation of equilibrium amounts of the tetragonal phase, but rather facilitates nucleation of the tetragonal phase in the form of nanometer-sized oblate spheroids in a cubic matrix (Figure 1.14). A subsequent subeutectoid heat treatment leads to growth of the tetragonal precipitates until they reach the size at which they can transform spontaneously to the monoclinic polymorph.

Normally, commercially available Mg-PSZ have rather complex microstructures, which consist of a coarse-grained cubic matrix (grains often on the order of tens of micrometers) with fine tetragonal and monoclinic grain boundary precipitates (Figure 1.15). The precipitates often transform during cooling to room temperature, and form the monoclinic phase; heterogeneously nucleated precipitates are often also formed within the grains. The fracture toughness of Mg-PSZ may be as high as 15 MPa $m^{1/2}$, but this will decrease with temperature. The fracture strength usually varies between 650 and 800 MPa.

Orthorhombic zirconia, which is also known as a "high-pressure polymorph," appears in Mg-PSZ when it is cooled to cryogenic temperatures [174]. In the nitrogen-quenched 9.4Mg-PSZ sample, the *ortho* phase is in the majority, at 46.6 ±

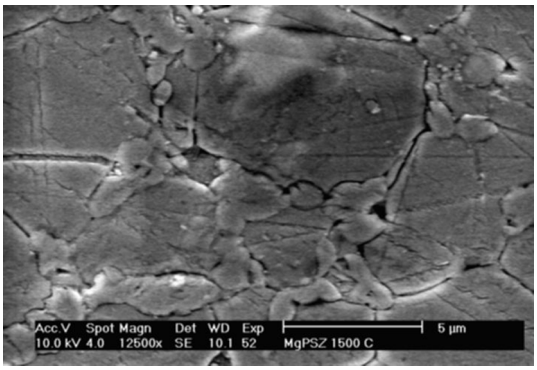

Figure 1.15 Microstructure of sintered and thermally aged Mg-PSZ consisting of large cubic grains and fine precipitates of tetragonal and monoclinic phases.

1.1 wt%. This material has a significantly higher Young's modulus (242 GPa, the second-highest of all zirconia-based materials, and the highest of all zirconia-based ceramics) than does the same material before cryogenic cooling; this is due to the very high modulus of the *ortho* phase, which is estimated to be ~285 GPa [181].

1.6.3.2 **Ca-PSZ**

Ca-PSZ is similar to Mg-PSZ, and develops similar microstructures during high-temperature aging. An important factor is the different critical size for unconstrained m → t transformation, which is approximately 6–10 nm for Ca-PSZ (compared to 25–30 nm for Mg-PSZ). An extensive systematic investigation of this material has been conducted by Garvie *et al.*, who achieved a considerable increase in the strength of the material, from 200 to 650 MPa, simply by ageing it at 1300 °C [182].

Various authors have reported different temperatures of eutectoid decomposition, ranging from 1000 to 1140 °C [183–185]. The eutectoid transformation is a rather slow process, and is therefore not seen in conventionally aged samples. However, a large cubic phase field also exists which, together with slow transformation, facilitates the existence of a fully cubic structure, providing the basis for calcia-stabilized zirconia solid electrolytes.

1.6.3.3 **Y-PSZ**

The addition of yttria to zirconia not only stabilizes the cubic or tetragonal form but also lowers the temperature of the t → m transformation. The practical consequence of this is that larger zirconia particles can be retained in the metastable tetragonal form, thus considerably easing any problems associated with the fabrication of a toughened ceramic, such as ZTA. One important feature of this system is the solubility of yttria in zirconia up to a concentration of approximately 2.5 mol% which, in conjunction with a low eutectoid temperature, will facilitate the formation of fully tetragonal ceramics which are referred to as "tetragonal zirconia polycrystals" (see Section 1.6.4).

A large cubic + tetragonal phase field in the Y_2O_3–ZrO_2 system permits the formation of a PSZ structure which is, in many respects, analogous to Mg-PSZ or Ca-PSZ, and consists of tetragonal precipitates embedded in a cubic phase matrix. The morphology of the precipitates depends on the conditions of ageing (e.g., time, temperature). For example, a rapid cooling will result in a displacive transformation and formation of the so-called t' phase, which has a lower c/a ratio than the normal tetragonal phase, and contains the same amount of yttria as the cubic phase [186].

1.6.3.4 **Ceria and Other Rare Earth-Stabilized Zirconias**

Ce-PSZ exhibits many similarities with Y-PSZ, having a very wide compositional range of formation of the solid solution of up to 18 mol% CeO_2. In the ZrO_2–CeO_2 system, the stabilization of t-ZrO_2 occurs over a wide composition range, from 12 to 20 mol% CeO_2, with a preferred composition of 12 mol% [187].

In order to obtain fully dense ceramics, it is necessary to use ultrafine powders that are normally prepared by the coprecipitation of precursors. The presence of liquid-forming additives, such as Ca and Si, is also often required. Although this material

achieves a very high fracture toughness, with reported values as high as 30 MPa · $m^{1/2}$, Ce-TZP is rarely used as a monolithic material due to its relatively low level of hardness and strength.

The ZrO_2–$GdO_{1.5}$ system is important for the development of ceramics for thermal barrier coatings (TBC), other than the state-of-the-art yttria-stabilized zirconia (YSZ), which has a lower thermal conductivity and improved high-temperature performance and durability [188].

Scandia-stabilized zirconia (ScSZ) possesses the highest oxygen-ion conductivity among all zirconia-based oxides, and therefore represents a promising solid electrolyte for applications in electrochemical devices such as solid oxide fuel cells (SOFCs) and catalytic membrane reactors (further details are available in Section 1.6.6.3).

The possibility of PrO_x–ZrO_2 solid solution formation has been hypothesized (despite the phase diagram being unknown) on the basis of the lanthania–zirconia phase diagram, and by considering the ionic radii of Zr^{4+} (0.87 Å) and both Pr^{3+} (1.126 Å) and Pr^{4+} (0.90 Å). When, recently, 10 mol% Pr-doped zirconia powders were prepared using a microwave-assisted hydrothermal synthesis, the doped powder was shown to be a substitutional solid solution of praseodymium in tetragonal zirconia [189].

1.6.4
Tetragonal Zirconia Polycrystals (TZP)

As the toughening effect in partially stabilized zirconias increases linearly with the amount of retained tetragonal phase, the logical consequence is the development of ceramics that are wholly tetragonal. This achievement was first accomplished by Rieth [190], and later by Gupta *et al.* [191], who prepared the ceramic by sintering yttria and other rare earth-containing zirconia powders in the temperature range 1400–1500 °C. The resultant ceramic was fine-grained, with a strength of 600–700 MPa. Moreover, the critical grain size for the t → m transformation was found to depend on the amount of stabilizing aids, this being about 0.2 μm for 2 mol % Y_2O_3 and 1.0 μm for 3 mol% Y_2O_3, as well as on the presence or absence of mechanical constraints. The typical properties of TZP are summarized in Table 1.9.

The microstructures of commercial TZP ceramics are usually far from ideal, and often contain a significant amount of the cubic phase. TZP ceramics also often contain amorphous grain boundary phases, generally low-viscosity liquids from the systems Al_2O_3–Y_2O_3–SiO_2. The presence of a liquid and a small grain size result in a pseudosuperplasticity of TZPs with an extension in tension of over 100% at 1200 °C. High-tensile ductility is attributed to grain size stability during high-temperature deformation [192], which is achieved by suppressing the grain growth by adding various oxides, such as CuO [193–195], Sc_2O_3 [196], and Al_2O_3 [197]. An elongation to failure of 520% has been achieved in 5 wt% SiO_2-added 8 mol% Y_2O_3-stabilized c-ZrO_2 (8YCZ) at 1430 °C [198]. The limited grain growth was not always an indispensable condition for superplastic ceramics. Moreover, the addition of TiO_2 increased the grain size but reduced the flow stress and enhanced the elongation to

Table 1.9 Typical properties of TZP.

Property		Value
Melting point		2720 °C
Bulk density		6.05 g cm^{-3}
Bending strength	RT	900–1300 MPa
	800 °C	350 MPa
Young's modulus		140–200 GPa
Fracture toughness		5.5–11 MPa $m^{1/2}$
Hardness		~14 GPa
Thermal conductivity (RT)		1–2 W m^{-1} K^{-1}
Coefficient of thermal expansion	100 °C	8.3×10^{-6} K^{-1}
	800 °C	10.5×10^{-6} K^{-1}
Thermal shock resistance		$\Delta T = 360$ °C

RT = room temperature.

failure [199]. It should be noted that this subject has been extensively reviewed by both Chokshi [200] and Jimenez-Melendo *et al.* [201].

One major obstacle against the full exploitation of TZP is the spontaneous surface t → m transformation that occurs when the ceramics are aged at temperatures of between 150 and 250 °C. The transformation is accompanied by a severe strength degradation, especially in a water vapor-containing environment, with the rate of degradation being governed by not only the number of oxygen vacancies but also the instability of *t*-ZrO_2. The aging rate was increased by about 50% in a 3Y-TZP dense sample sintered under reducing conditions, in comparison to a similar sample which had been sintered in air (Figure 1.16) [202]. Ageing is inhibited by the addition of liquid-forming additives, especially silica [203], and also by the addition of CeO_2 or

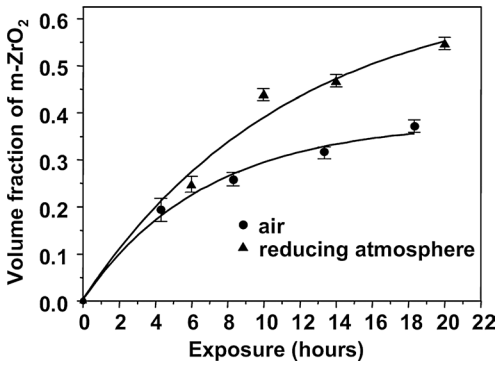

Figure 1.16 Surface monoclinic phase fraction versus exposure time at 140 °C in steam for the zirconia materials sintered in air and in a 90% Ar/10% H_2 atmosphere [202].

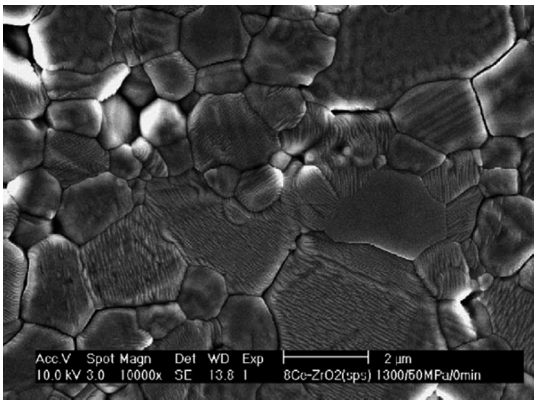

Figure 1.17 Scanning electron microscopy image of the 8 mol% CeO_2-stabilized ZrO_2 ceramic after spark plasma sintering [210].

Al_2O_3 [204, 205]. Al_2O_3 also raises the CeO_2 content in ZrO_2 grains, thus preserving a more tetragonal phase and enhancing the fracture toughness [206].

The applicability of Ce-TZP is limited also by its susceptibility to the reduction of Ce^{4+} to Ce^{3+} when sintering or using the ceramics in a nonoxidizing atmosphere. The reduction is accompanied by a change in color [207, 208]. Due to increases in the ionic radius of the cerium ions, from 0.101 nm for Ce^{4+} to 0.111 nm for Ce^{3+}, there is an approximate 40% mismatch in ionic radius with Zr^{4+}, and this results in a high elastic lattice strain and the segregation of Ce^{3+} to the grain boundaries [209]. Consequently, tetragonal ZrO_2 will be destabilized and cracking will occur in the bulk material. The sintering of Ce-TZP in nitrogen, or the hot isostatic pressing of presintered materials in a reducing environment with graphite heating elements, is not possible as the tetragonal phase is completely destabilized and transforms to monoclinic during cooling [207]. High heating rates and short soaking times, facilitated by SPS, partially overcomes this obstacle, such that Ce-PSZ consisting of monoclinic and tetragonal ZrO_2 with a volume ratio of 2 : 1, and a trace amount of Zr–Ce–O cubic solid solution, were prepared using this method (Figure 1.17) [210].

Both, Ce-TZP [211] and Ce–Y-TZP [212] exhibit martensitic transformation-associated shape memory. For example, the 8Ce–0.50Y-TZP exhibits a complete shape memory recovery under a recoverable strain of 1.2% at a relatively high operating temperature (>500 °C) [213].

1.6.5
Zirconia-Toughened Alumina (ZTA)

In the past, zirconia has been added routinely to a variety of ceramic materials in order to increase their toughness. Zirconia-toughened alumina was first developed by Claussen, who demonstrated a significant toughening effect of unstabilized, but transformable, tetragonal zirconia particles within the alumina matrix [214].

The retention of such particles is facilitated by mechanical constraints imposed by the surrounding alumina matrix with a high elastic modulus. Both, the transformation toughening and microcracking, contribute to increasing the fracture toughness of alumina. Unstabilized ZTAs can achieve the bending strength of up to 1200 MPa, and a fracture toughness of about 16 MPa $m^{1/2}$ at 15 vol% ZrO_2.

1.6.6 Applications of Zirconia

1.6.6.1 Thermal Barrier Coatings

The efficiency of gas turbine engines is dictated by the maximum temperature that the turbine rotors can sustain during continuous operation. If a thin coating of ceramic is supplied to a metal turbine blade, then the engine temperature can be increased by 50–200 °C, without increasing the temperature of metal. The desirable properties of a suitable ceramic thermal barrier coating include a high thermal expansion (close to that of metal), a low thermal conductivity, chemical stability in the gas turbine environment, and a high thermal shock resistance [215].

Plasma-sprayed zirconia coatings of PSZ composition (namely YSZ) deposited by electron beam physical vapor deposition (EB-PVD) and atmospheric plasma spraying (APS) have been investigated for this purpose. The microstructure of sprayed coatings is nonequilibrium and fine-grained, and contains both macrocracks and microcracks and a residual porosity. As a result, sintering through crack healing, accompanied by grain growth, takes place at elevated temperatures [216, 217]. Sintering affects the mechanical and physical properties, namely elastic modulus, strength and work of fracture, and also increases the thermal conductivity and impairs the strain-tolerant capability of TBCs. An increase in long-term phase, mechanical, and chemical stability under working conditions is therefore of primary importance. The chemical attack of coatings by the mineral constituents of fuel, especially Na, Mg, and S (in the form of liquid sulfates) and vanadium, deplete the YSZ coatings of yttrium, with subsequent destabilization and deterioration of the mechanical properties [218]. A review of mechanical behavior of YSZ-based thermal barrier coatings is provided in Ref. [219].

A decrease in thermal conductivity and an increase in thermal protection are achieved by adjusting the microstructure and porosity of ZrO_2–Y_2O_3 (7–8) wt% coatings [220–222]. The defect-cluster design approach, using high-stability, paired dopant oxides of distinctively different ionic sizes, produces lattice distortion in the oxide solid solutions, and also facilitates local ionic segregation and defect clustering. Oxide defect clusters with appropriate sizes attenuate and scatter the lattice and radiative phonon waves over a wide range of frequencies. The formation of thermodynamically stable, highly defective lattice structures with controlled defect-cluster sizes reduces oxide intrinsic lattice and radiation thermal conductivity. The influence of codoping with additional paired rare earth oxides Nd_2O_3–Yb_2O_3 or Gd_2O_3–Yb_2O_3 (i.e., ZrO_2–$(Y,Nd,Yb)_2O_3$ and ZrO_2–$(Y,Gd,Yb)_2O_3$) on thermal conductivity is shown in Figure 1.18 [215].

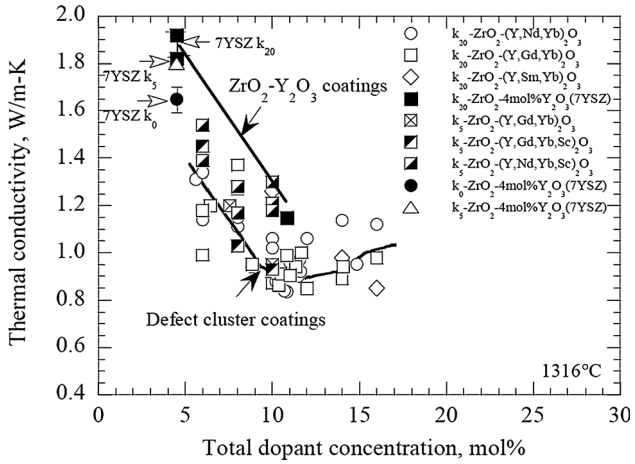

Figure 1.18 Thermal conductivity of various composition electron beam physical vapor deposition oxide defect-cluster coatings as a function of total dopant concentration [215].

The disadvantages of YSZ at high temperatures prompted an intense search for new TBC materials (for reviews on recent developments, see Refs [223, 224]). Interesting candidates for TBCs include zirconia-based materials with a pyrochlore structure and a high melting temperature, such as $La_2Zr_2O_7$, $Gd_2Zr_2O_7$, or $Nd_2Zr_2O_7$. Although these materials have a lower thermal conductivity and a higher thermal stability than YSZ, their thermal expansion is usually lower than that of YSZ, which leads to higher thermal stresses in the TBC. In addition, their toughness is lower due to an absence of toughening effects [225]. However, this problem can be solved by the use of layered topcoats; in this case, YSZ is used as a TBC material with a relatively high thermal expansion coefficient and high toughness. The YSZ layer is then coated with a new TBC material (e.g., $La_2Zr_2O_7$) which is then able to withstand higher temperatures (by about 100 °C) [226].

1.6.6.2 **Solid Electrolytes**

The use of zirconia as a solid electrolyte (and especially for oxygen-sensing devices) is facilitated by the fact that stabilized zirconia has a defect structure with a finite concentration of octahedral interstitial voids. The void space in the lattice is larger for the O^{2-} anions than for the Zr^{4+} cations, and the O^{2-} anions are therefore the rate-controlling species in the diffusion process.

The maximum ionic conductivity in ZrO_2-based systems is achieved when the concentration of acceptor-type dopant(s) is close to the minimum necessary for complete stabilization of the cubic fluorite structure [227, 228]. For example, the highest conductivity in $Zr_{1-x}Y_xO_{2-x/2}$ and $Zr_{1-x}Sc_xO_{2-x/2}$ ceramics is achieved at $x = 0.08$–0.11 and 0.09–0.11, respectively. Further additions decrease the ionic conductivity due to an increasing association of the oxygen vacancies and dopant cations into complex defects of low mobility [229]. This effect is more pronounced

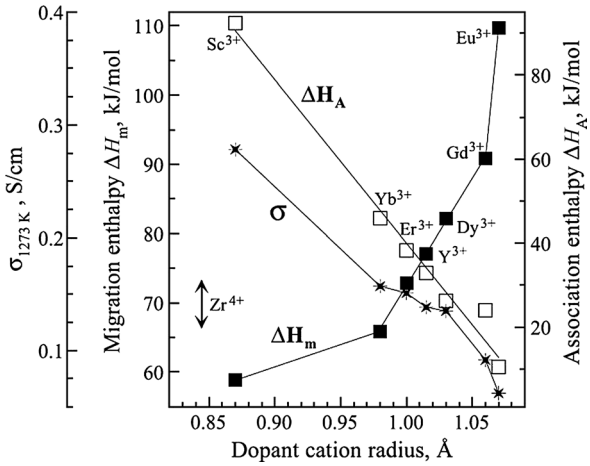

Figure 1.19 Maximum conductivity in the binary ZrO_2–Ln_2O_3 systems at 1000 °C, and the oxygen-ion migration and association enthalpies versus radius of Ln^{3+} cations [243].

if the mismatch between the host and dopant cation radii is larger [230, 231] (Figure 1.19). Because the Zr^{4+} ion is smaller than the trivalent rare earth cations, a maximum ionic transport is observed for Sc^{3+}. However, due to the high cost and problems with the ageing of Sc-FSZ at moderate temperatures, Y-FSZ is used for most practical applications.

The doping of ZrO_2 with alkaline earth metal cations (A^{2+}) is less effective due to a greater tendency to defect association and to a lower thermodynamic stability of the cubic fluorite-type solid solutions in ZrO_2–AO systems. To date, attempts to increase the stability of Sc-containing materials by codoping, or to reduce the cost of Ln^{3+}-stabilized phases by mixing them with cheaper alkaline earth dopants, have not yielded any worthwhile results [228].

Commercially available zirconia electrolytes often contain secondary phases, especially alumina- and silica-containing precipitates. The presence of a grain boundary glass causes a deterioration in the electrical properties due to its poor ionic conductivity [232], and a significant increase in grain boundary resistance [233–235]. In contrast, the minor addition of a highly dispersed Al_2O_3 decreases the grain boundary resistance by scavenging silica-rich impurities into new phases that do not wet the grain boundaries [236–238]. Moreover, the addition of alumina increases the mechanical strength by retarding grain growth. A similar effect was observed in Mg-PSZ, where MgO reacts with silica and forms discrete forsterite grains within the zirconia matrix [239]. Also, if the admixed MgO amount exceeds the solubility limit, then MgO will form a second phase in the zirconia matrix after sintering. Then, the MgO has a higher electrical conductivity than zirconia, and the conductivity of the composite electrolytes is therefore correspondingly higher [240].

The achievement of a high ionic conductivity in nanostructured ZrO_2 is questionable. In some studies, the overall conductivity of nanocrystalline YSZ ceramics was found to be comparable to that of their microcrystalline counterparts [241].

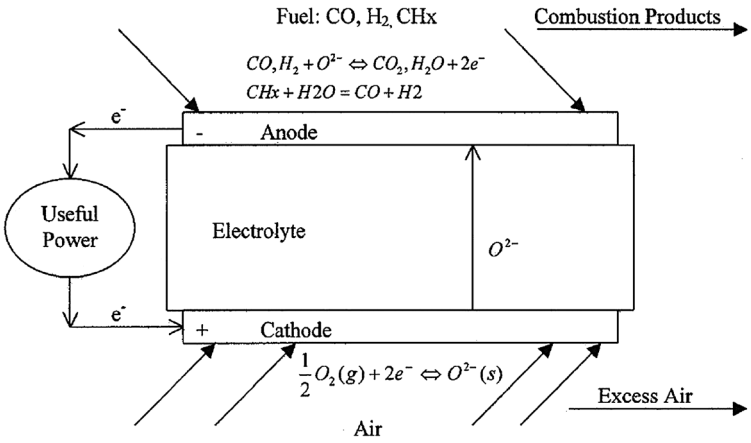

Figure 1.20 Schematic diagram of a fuel cell using a zirconia electrolyte [254].

In contrast, an increase in conductivity by about one order of magnitude was reported in YSZ nanostructured thin films [242] (for a review on this topic, see Ref. [229]).

1.6.6.3 **Fuel Cells**

The ionic conductivity of stabilized zirconia is utilized in solid oxide electrolyte fuel cells, as pioneered by Westinghouse in 1986. These cells function in reverse to a hydrogen generator, at temperatures approaching 1000 °C (Figure 1.20), with the diffusion of oxygen ions through a zirconia electrolyte. This is usually in the form of a tube, with air passing along one surface and the fuel (usually hydrogen) along another surface, which facilitates oxidation to proceed on the anode. The ionization of an oxygen molecule takes up to four electrons to the cathode, thus generating an electrical current in conjunction with oxidation of the fuel.

Current efforts are aimed at lowering the operating temperature of SOFCs from above 900 °C down to 500 °C, in order to improve both the longevity and cost of the peripheral materials and the electrical power generation efficiency [244]. Tetragonal zirconia is considered to be an electrolyte for intermediate-temperature solid oxide fuel cells (IT-SOFCs), due to better mechanical and electrical properties at lower temperatures in comparison with cubic zirconia [245]. Dense YSZ thin-film-based SOFCs can be operated at intermediate temperatures (650–800 °C), achieving power densities of between 0.35 and 1.9 W cm^{-2}, depending on the temperature and film thickness [246, 247]. Scandia-stabilized zirconia (ScSZ) has a higher ionic conductivity than YSZ, and a high mechanical strength and fracture toughness, which increases the reliability of ScSZ-based SOFCs [248–250]. ScSZ electrolyte sheets and electrolyte-supported-type cells have been designed for reduced-temperature operation (ca. 800 °C). However, for the working temperature range of the low-temperature SOFC (600–800 °C), the temperature dependence of electrical conductivity changes drastically across a composition boundary at approximately 10 mol% Sc_2O_3. At additive levels of between 3 and 8 mol%, the electrical conductivity changes smoothly with temperature, but at a content above 12 mol% a discontinuity of

electrical conductivity appears at 650 °C, above which temperature a highly conductive cubic phase prevails. Below 650 °C, a less-conductive rhombohedral h-phase ($Zr_7Sc_2O_{17}$) is formed [251, 252].

One problem here is the low-temperature degradation and deterioration of mechanical properties under hydrothermal conditions, due to the t → m transformation of zirconia. This makes the application of t-ZrO_2 in IT-SOFC devices challenging, as water vapor is produced at the anode when the cell is in operation. The fuel cell must also be able to withstand thermal cycling, and to operate under pressures greater than atmospheric over the lifetime of the cell (>50 000 h) [253].

1.6.6.4 **Bioceramics**

Biomedical-grade zirconia was introduced 20 years ago to solve the problem of alumina brittleness, and the consequent potential failure of implants. The reason for this is that biomedical-grade zirconia exhibits the best mechanical properties of oxide ceramics as a consequence of transformation toughening, which increases its resistance to crack propagation. Likewise, partially stabilized zirconia shows excellent biocompatibility, and it has therefore been applied to orthopedic uses such as hip and knee joints [255].

The metastability of zirconia – and especially of Y-TZP, which is prone to ageing in the presence of water – represents a serious problem in biomedical applications [256]. Yttrium, as a trivalent ion, creates oxygen vacancies that aid hydroxyl group diffusion in the lattice, generating nucleation of the transformation via a stress corrosion-type mechanism [257]. The resultant degradation is characterized by surface roughening, microcracking at the surface, and the release of particles into the body. Although the manufacturers of zirconia claimed that this problem was limited under *in vivo* conditions, in the year 2001 approximately 400 implanted femoral heads constructed from zirconia failed within a very short period. Consequently, the aging and wear of zirconia has become a very important issue, the main aim being to renew the confidence of the medical community in zirconia-based biomaterials.

As shown in Figure 1.21, the aging-related nucleation and phase transformation leads to a cascade of events. The transformation of one grain, associated with a

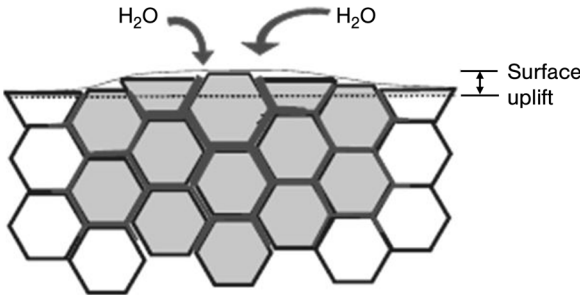

Figure 1.21 Schematic of the transformed zone in aged biomedical-grade zirconia, leading to extensive microcracking and surface roughening. The transformed grains are shown in gray. The dark gray path represents the penetration of water due to microcracking around the transformed grains [257].

volume increase, stresses the neighboring grains and results in the formation of microcracks; this, in turn, creates a pathway through which water can penetrate further into the material. The initial transformation of individual grains is process-related, and depends on their disequilibrium state – that is, the size of the grains and the content of the stabilizing aid [256], the specific orientation from the surface [258], the presence of residual stresses, and/or even the presence of a cubic phase [259]. The slowing down or even prevention of such aging is of the utmost importance, with proposed solutions including the addition of small amounts of silica [260] or the use of yttria-coated rather than coprecipitated powders [261]. Another possibility would be to use Ce-doped zirconia, as this material exhibits superior toughness (up to $20\,\mathrm{MPa}\cdot\mathrm{m}^{1/2}$) and negligible aging during the lifetime of an implant [257].

Due to the above-mentioned problems, the use of zirconia-based biomaterials in the surgery of large bones is currently restricted, and the manufacturers have responded by developing a series of toughened composites. These include an alumina-toughened zirconia (Bio-Hip®; Metoxit AG, Thayngen, Switzerland), which has a bending strength of up to 2000 MPa, and a zirconia-toughened alumina (BIOLOX®delta; Ceramtec AG, Plochingen, Germany) with a bending strength in excess of 1150 MPa and a fracture toughness of $\sim 8.5\,\mathrm{MPa}\cdot\mathrm{m}^{1/2}$.

1.7
Cerium Oxide

Cerium oxide (CeO_2) has found numerous applications as an electrolyte for SOFCs, as abrasive materials for chemical mechanical planarization (CMP), as a UV absorbent, as a material for oxygen pumps, and as an automotive exhaust promoter.

1.7.1
Crystal Structure and Properties of Single-Crystal CeO_2

Cerium is a common, naturally occurring element that is characterized chemically by having two valence states, $+3$ and $+4$. Ce^{4+} is the only nontrivalent rare-earth ion that is stable in an aqueous environment and it is, therefore, a strong oxidizing agent. The $+3$ state closely resembles the other trivalent rare earths.

Cerium oxide is a highly stable, nontoxic, refractory ceramic material with a melting point of 2600 °C and a density of $7.13\,\mathrm{g\,cm^{-3}}$. Ceria has a fluorite face-centered cubic crystal structure with a lattice constant of 5.11 Å (Figure 1.22). CeO_2 easily transforms from the stoichiometric CeO_2 ($+4$) state to the Ce_2O_3 ($+3$) valence state via a relatively low-energy reaction, although even at a loss of considerable amounts of oxygen from the crystal lattice, and the formation of a large number of oxygen vacancies, its fluorite structure is retained. The suboxides thus formed may be readily reoxidized to CeO_2 in an oxidizing environment.

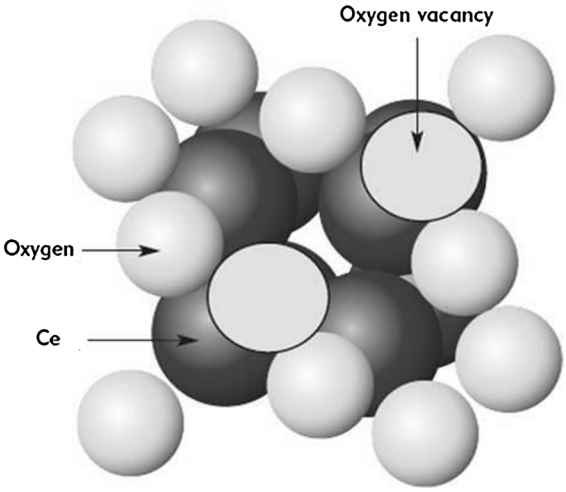

Figure 1.22 Fluorite structure of CeO_2.

1.7.2
Natural Sources and Production

The two largest sources of cerium and other rare earth elements are the minerals *bastnasite* and *monazite*. Bastnasite, which belongs to carbonate-fluoride minerals, exists as several types: bastnasite-(Ce) (Ce, La)CO_3F; bastnasite-(La) (La, Ce)CO_3F; and bastnasite-(Y) (Y, Ce)CO_3F. The most frequently occurring of these is bastnasite-(Ce), and cerium is by far the most common of the rare earths in this class of minerals.

Cerium oxide is extracted from bastnasite by roasting the ore with concentrated sulfuric acid, or with sodium carbonate [262]. Since, in the first process, HF forms as a byproduct, roasting with sodium carbonate is the preferred method. The rare earth elements contained in calcine are extracted by leaching with hydrochloric acid, and recovered from the leachate by precipitation with oxalic acid. During the course of roasting, cerium(III) is oxidized to cerium(IV). CeO_2 is insoluble in dilute hydrochloric acid; this is in contrast to other trivalent rare earth elements, which can be easily leached out, as can the impurities such as Fe, Ca, and Mg.

The present applications of ceria-based ceramics impose strict requirements on the quality and purity of the powders used. Several studies have described the synthesis of ceria nanopowders of high quality and with a well-defined morphology. Typical methods of preparation include hydrothermal synthesis [263, 264], the hydrolysis of an alkoxide solution (sol–gel) [265], chemical precipitation [266], mechanochemical processing [267], and gas-phase reaction [268]. *Emulsion techniques* can also be used, as these reduce not only the production costs of high-purity spherical powders but also the degree of aggregation. Thus, ceria powders with an average particle size <20 nm and a narrow particle size distribution can be

prepared by reaction between two emulsions containing cerium nitrate and an alkaline precipitation agent, such as ammonium hydroxide or sodium hydroxide [269].

1.7.3 Properties

The mechanical properties of undoped ceria ceramics are usually rather poor; typically, these materials have room-temperature bending strengths of ~100 MPa and a fracture toughness of $\sim 1.5\,\mathrm{MPa}\cdot\mathrm{m}^{1/2}$ [270]. The fracture toughness of $Ce_{0.8}Gd_{0.2}O_{2-\delta}$ ceramics has been reported as $1.5 \pm 0.2\,\mathrm{MPa}\cdot\mathrm{m}^{1/2}$, this being independent of the crack length or grain size, within the range of 0.5 to 9.5 μm [271]. Such grain size-independence of fracture toughness is attributed to the almost 100% transgranular nature of the fracture of doped ceria ceramics. The bending strength is, in some cases, improved by the addition of other rare earth oxides [272], while the fracture strength is influenced by the method used to prepare the starting powder (Figure 1.23), the temperature of sintering, and by the concentration rather than the type of dopant (Figure 1.24). These ceramics fail transgranularly, with the proportion of the transgranular fraction ranging between 96% and 99%. The variation in fracture strength is attributed to the decrease in transgranular strength due to the generation of oxygen vacancies introduced by dopants, which distort the lattice and decrease the coulombic forces between ions [273].

As an ionic conductor (exhibiting a high mobility of oxygen ions), ceria represents a major candidate material for SOFCs. Microcrystalline ceria doped with various rare earth elements has a higher ionic conductivity than does stabilized ZrO_2, especially at lower temperatures. As ceria also exhibits electronic conductivity, it is in fact a mixed ionic–electronic conducting material, with ionic conductivity prevailing at temperatures above 500 °C. The high electronic conductivity of undoped nanocrystalline ceria is attributed to electronic conduction along the grain boundaries [274, 275].

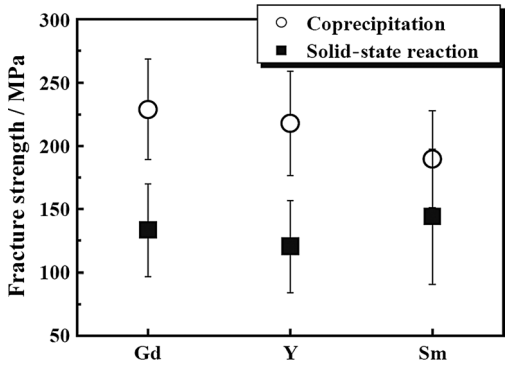

Figure 1.23 The fracture strength of $(CeO_2)_{0.80}(LnO_{1.5})_{0.20}$ (Ln = Y, Gd, and Sm) ceramics prepared by solid-state reaction of CeO_2 and the respective rare earth oxide powder and by an oxalate coprecipitation method [272].

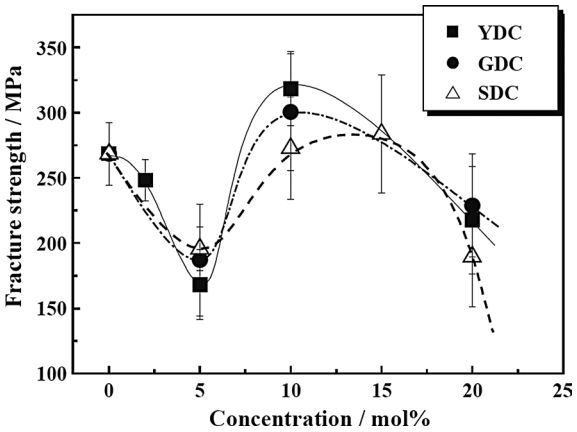

Figure 1.24 Dependence of room temperature fracture strength of doped CeO_2 ceramics on the concentration of rare earth-dopants: yttrium (YDC), gadolinium (GDC), and samarium (SDC). [272].

1.7.4 Applications

1.7.4.1 Abrasives

Because of its high chemical activity and unique crystal structure, cerium oxide is used as a polishing powder, the advantages of which include a long life, a high polishing efficiency, and a low residua. Today, ceria is gradually replacing traditional abrasives for some applications. Ceria polishing powders are classified as two types: (i) high-cerium abrasives with a ceria content >80%; and (ii) low-cerium abrasives with a ceria content of 48–50%. Currently, cerium oxide abrasive powders with nanosized spherical particles and a narrow particle size distribution are used for the chemical mechanical planarization of semiconductor devices, in order to reduce the scratching of wafers [276].

1.7.4.2 Solid Electrolytes

The main obstacle against the use of ceria in SOFCs is the partial reduction of Ce^{4+} to Ce^{3+} [277, 278]. Under the reducing conditions experienced on the anode side of the fuel cell, a large number of oxygen vacancies is formed within the ceria electrolyte, and consequently CeO_2 is reduced to Ce_2O_3, thus increasing electronic conductivity of the material. Finally, as a result of the oxygen vacancy formation, ceria undergoes a so-called "chemical expansion." The high ionic conductivity encountered at lower temperatures, coupled with problems related to the reduction, limit the application of ceria electrolytes at relatively low temperatures.

Due to the small association enthalpy between the dopant cation and oxygen vacancy in the fluorite lattice, the highest conductivity is achieved in ceria doped with Gd^{3+} or Sm^{3+} [279, 280]. The highest level of oxygen ionic transport is found in the solid solutions $Ce_{1-x}Ln_xO_{2-\delta}$, where Ln = Gd or Sm, and $x = 0.10$–0.20. The lattice ionic conductivity of Ln-doped ceria is about $0.01\ S\,cm^{-1}$ at 500 °C; however, the

substitution of a fraction of the ceria with Gd or Sm introduces vacancies without adding any electronic charge carriers. This has two main consequences: (i) it provides an n-type electronic conductivity which causes a partial internal electronic short circuit in a cell; and (ii) it generates nonstoichiometry with respect to normal valency in air and an expansion of the lattice, which can lead to mechanical failure. The effect of lattice expansion on mechanical integrity depends on the geometry of the cell, and the way in which the ceria is supported. In general, ceria electrolytes are considered to be mechanically unstable at temperatures above 700 °C [281].

The grain boundaries are of profound importance for the ionic conductivity, as they partially block ionic transport so that the total resistance will depend on the level of segregated impurities. The properties of CeO_2-based solid electrolytes have been reviewed elsewhere [229, 282–284].

Doped ceria is only viable for operating temperatures below 600 °C, and is therefore normally used as a supported thick film. In order to preserve a high activity and to maintain compatibility with metal supports, the processing temperature should be kept as low as possible (e.g., 1000 °C), although this may be difficult to achieve due to the high refractoriness of ceria. Consequently, small amounts (e.g., 1 mol%) of oxides of divalent transition metals (e.g., Co, Cu, Mn) are often used as sintering aids for Gd-doped ceria [285–287]. Unfortunately, CuO, CoO and MnO_2 partially impair the grain boundary conductivity by promoting the propagation of SiO_2 impurities at the grain boundaries [286, 287]. The addition of a small amount of Fe_2O_3 (~0.5 atom%) will reduce the sintering temperature by ~200 °C and also promote densification. Iron is also believed to promote the dissolution of Gd_2O_3 in CeO_2 at lower sintering temperatures, and to increase the grain boundary conductivity by scavenging the SiO_2. In general, the concentration of the transition metal sintering aids must be kept as low as possible in order to minimize their influence on the ionic or electronic performance of the electrolyte [285, 288].

Highly reactive nonagglomerated powders can be sintered to high density at low temperatures, without the need for additives. Fully dense ceramics with grain sizes between 0.15 and 0.75 μm were prepared via a pressureless sintering of Sm-doped nanopowders (14 nm) at 1000 °C [289].

1.7.4.3 **Catalysts**

Cerium oxide is used in exhaust three-way catalytic converters where the emissions from fuel burning are converted to harmless gases. The conversion includes the following reactions:

Hydrocarbon combustion:

$$(2x+y)CeO_2 + C_xH_y \rightarrow [(2x+y)/2]Ce_2O_3 + x/2CO_2 + y/2H_2O \quad (13)$$

Soot burning:

$$4CeO_2 + C_{soot} \rightarrow 2Ce_2O_3 + CO_2 \quad (14)$$

NO_x reduction:

$$Ce_2O_3 + NO \rightarrow 2CeO_2 + 1/2N_2 \quad (15)$$

The catalytic activity of cerium oxide depends on its particle size and surface area. As oxygen vacancy atomic point defects are formed more easily at the surface than in the bulk, high-surface-area materials will have a substantially higher catalytic activity [290]. The activation temperature of carbon combustion is reduced from approximately 700 °C for a micron-sized material to 300 °C, if the surface area of the material is increased by a factor of 20 [291].

1.8 Yttrium Oxide

Although yttrium oxide is rarely used as a ceramic material in its pure form, it is widely applied as an additive in various ceramics, where it is used as a component of sintering aids (e.g., in silicon nitride, or alumina), as a stabilizer in zirconia and in alumina-zirconia abrasives, in wear-resistant and corrosion-resistant cutting tools, seals and bearings, high-temperature refractories for continuous-casting nozzles, jet engine coatings, oxygen sensors in automobile engines, as a component of high-temperature superconductors of the Y–Ba–Cu–O composition, and in artificial gemstones. In electronics, yttrium–iron–garnets are used as components in microwave radars for the control of high-frequency signals. With aluminum oxide, yttrium forms yttrium–aluminum garnet, which is used in solid-state lasers. The use of yttrium oxide in its pure form, although less extensive, is described in greater detail in Section 1.8.4.

1.8.1 Crystal Structure and Properties of Single Crystal Yttrium Oxide

Yttrium oxide is a white refractory crystalline solid with a melting point of 2410 °C and a density of 5.03 g cm^{-3}. Yttrium oxide has a cubic, body-centered crystal lattice with the lattice parameter $a = 10.604$ Å, and with yttrium atoms octahedrally coordinated with six oxygen atoms. The cubic yttria undergoes a polymorphic phase cubic $\rightarrow$ hexagonal transition at about 2350 °C [292]. The H-type with space group D_{6h}^4 is a high-temperature hexagonal phase.

1.8.2 Natural Sources and Preparation

Yttrium is found together with other rare earth oxides in monazite sands [(Ce, La, etc.)PO_4] and in bastnasite [(Ce, La, etc.)(CO_3)F] (see Section 1.7.1). Yttrium is extracted together with other rare earth elements in a concentrated solution of sodium hydroxide at 140–150 °C; after cooling, the hydroxides of the rare earth elements are separated by filtration. Alternatively, bastnasite may be calcined to drive off CO_2 and fluorine, and then leached with hydrochloric acid to dissolve the trivalent rare earth elements. The rare earth hydroxides and chlorides obtained in this way are further processed to produce individual rare earth metal compounds

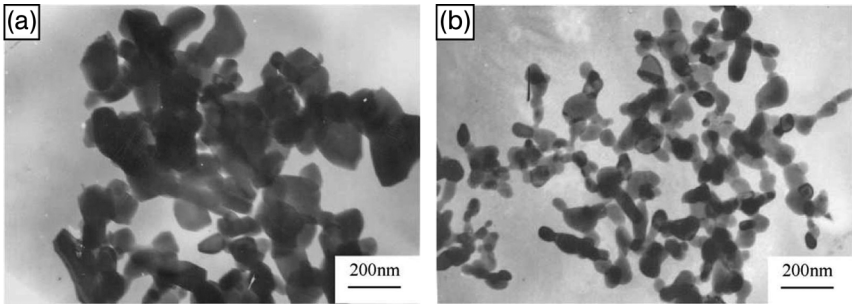

Figure 1.25 Morphology of yttria powder prepared by the precipitation of yttrium nitrate (a) without the addition of SO_4^{2-} and (b) with the addition of SO_4^{2-} [299].

such as fluorides, nitrates, carbonates, oxides, and pure metals for a variety of applications.

Ultra-fine-grained highly reactive yttria powders, suitable especially for the preparation of transparent ceramics, are prepared by various methods including combustion synthesis [293], precipitation [294, 295], hydrothermal synthesis [296], electrospray pyrolysis [297], and sol–gel [298]. In order to improve the dispersion and sinterability of yttria powders, seed crystals are often added [296]. A significant refinement of yttria powders prepared by precipitation from solution may be achieved by the addition of sulfate ions to the reaction mixture [299] (Figure 1.25).

Polycrystalline yttria ceramics are usually prepared by the conventional sintering of yttrium oxide powders [300, 301]. Due to its high refractoriness, yttrium oxide is rather difficult to sinter at ambient pressure. Even in a vacuum, the onset of densification of standard micrometer-sized powders occurs between 1400 and 1650 °C, while the achieved densities are low and the grain growth rapid (~65%) [302]. The use of sintering additives such as La_2O_3 [303], LiF [304] and ThO_2 [305], or the application of a high temperature (>2000 °C) [306] and pressure [307], are required for complete densification when fabricating fully dense or transparent yttria. The complete elimination of any residual porosity at lower temperatures, and refinement of the microstructure, can be achieved by hot isostatic pressing, which results in a material with a greater hardness, flexural strength, and thermal shock resistance (Figure 1.26) [308]. A fully dense nanocrystalline yttria with a grain size of 60 nm was recently prepared using a pressureless, two-stage sintering of a yttria nanopowder without additives at a temperature of about 1000 °C [309].

1.8.3 Properties

The use of yttria ceramics as standalone materials for structural applications is rather limited by their poor mechanical properties. For example, the commercially available 99.9% polycrystalline yttria Ceralloy® (Ceradyne Inc.) has a flexural strength of 99 MPa, a hardness of 5.85 GPa, and a fracture toughness of 1.4 MPa $m^{1/2}$. The hardness and fracture toughness of polycrystalline yttria are virtually grain-size

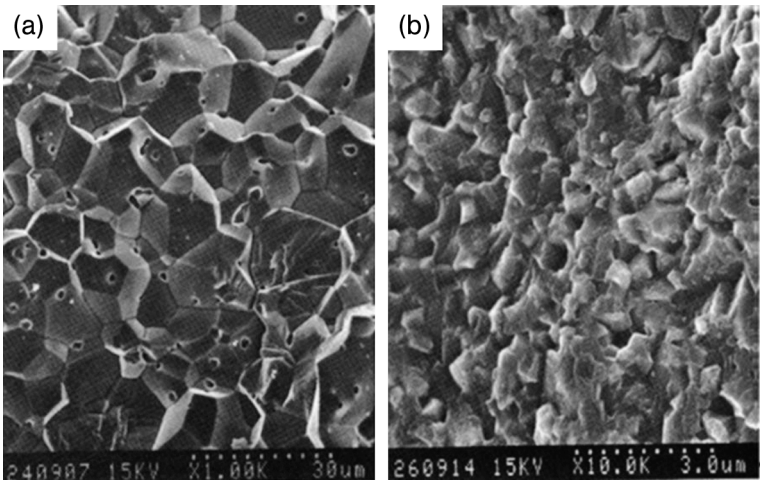

Figure 1.26 The microstructure of dense yttrium oxide prepared by (a) vacuum sintering and (b) hot isostatic pressing [308].

independent, with measured values being almost constant among all materials with grain sizes between 0.2 and 214 μm [310]. The fracture properties of yttria ceramics are influenced by the stoichiometry; a maximum fracture toughness of 3.5 $MPa \cdot m^{1/2}$ is achieved at stoichiometric composition, but this decreases to 2.3 $MPa \cdot m^{1/2}$ in an oxygen-deficient material. Such a change is reversible, however, with the initial value being restored after oxidation, and the hardness experiencing only a minor variation [311].

The Poisson ratio of yttria is 0.31, and the elastic modulus 170 GPa. The material has a relatively high thermal expansion coefficient ($9.1 \times 10^{-6}\,K^{-1}$), which is comparable to that of polycrystalline alumina, and a high thermal conductivity ($14\,W\,mK^{-1}$), which is twice that of the other solid-state laser host material, $Y_3Al_5O_{12}$ (YAG). Yttria has also a very high electrical resistivity ($10^{14}\ \Omega \cdot cm$), is refractory by nature, is highly chemically and thermally stable, and is optically clear over a broad spectral region.

1.8.4 Applications

Three decades ago, Greskovich and Chernoch created a new field of application of yttria by producing a laser yttria host-based ceramic material [312]. Yttria is not only used as a solid-state laser material as a laser host crystal for trivalent lanthanide activators, such as Yb^{3+} and Nd^{3+}, but also shows significant potential for luminous pipes in high-intensity discharge lamps and heat-resistive windows.

As an optical ceramic, yttrium oxide transmits well in the IR range, from 1 to 8 μm wavelength. This high IR transmission, together with a good resistance to erosion and thermal shock, means that yttrium oxide would serve as an ideal material for protection domes for IR sensors [313].

Due to its high thermodynamic stability, yttria is used for the protective coatings of high-temperature containers or structural components intended for use in reactive environments (especially molten metals, such as titanium or uranium). In effect, the reactive material is in contact with the thin economical layer of Y_2O_3, while the container substrate is prevented from coming into direct contact with the molten metal. As a result, a double protection is achieved – that of the container against corrosion, and of the melt against container-originating impurities. Due to its high refractoriness and low neutron absorption, yttria may also be used as a structural material for nuclear reactors.

References

1 Cowley, J.D. and Lee, W.E. (2005) Materials Science and Technology; A Comprehensive Treatment; Chapter 2, Oxide Ceramics, in *Structure and Properties of Ceramics*, vol. 11 (ed. M. Swain), Wiley-VCH Verlag GmbH, Weinheim, Germany, pp. 87–91.

2 Borsella, E., Botti, S., Giorgi, R., Martelli, S., Turtù, S., and Zappa, G. (1993) *Appl. Phys. Lett.*, **63**, 1345.

3 Kumar, P.M., Borse, P., Rohatgi, V.K., Bhoraskar, S.V., Singh, P., and Sastry, M. (1994) *Mater. Chem. Phys.*, **36**, 354.

4 Hirayama, T. (1987) *J. Am. Ceram. Soc.*, **70**, C122.

5 Kumar, P.M., Balasubramanian, C., Sali, N.D., Bhoraskar, S.V., Rohatgi, V.K., and Badrinarayanan, S. (1999) *Mater. Sci. Eng.*, **B63**, 215.

6 Chen, Y., Glumac, N., Kear, B.H., and Skandan, G. (1997) *NanoStruct. Mater.*, **9**, 101.

7 Skandan, G., Chen, Y.-J., Glumac, N., and Kear, B.H. (1999) *NanoStruct. Mater.*, **11**, 149.

8 Almyasheva, O.V., Korytkova, E.N., Maslov, A.V., and Gusarov, V.V. (2005) *Inorg. Mater.*, **41**, 540.

9 Yoldas, B.E. (1975) *Am. Ceram. Soc. Bull.*, **54**, 289.

10 Ji, L., Lin, J., Tan, K.L., and Zeng, H.C. (2000) *Chem. Mater.*, **12**, 931.

11 Rao, G.V.R., Venkadesan, S., and Saraswati, V. (1989) *J. Non-Cryst. Solids*, **111**, 103.

12 Sharma, P.K., Varadan, V.V., and Varadan, V.K. (2003) *J. Eur. Ceram. Soc.*, **23**, 659.

13 Dhara, S. (2005) *J. Am. Ceram. Soc.*, **88**, 2003.

14 Karagedov, G.R. and Lyakhov, N.Z. (1999) *NanoStruct. Mater.*, **11**, 559.

15 Wang, Y., Suryanarayana, C., and An, L. (2005) *J. Am. Ceram. Soc.*, **88**, 780.

16 Bae, S.I. and Baik, S. (1993) *J. Mater. Sci.*, **28**, 4197.

17 Hansen, S.C. and Philips, D.S. (1983) *Philos. Mag. A*, **47**, 209.

18 Harmer, M. (1984) *Adv. Ceram.*, **10**, 679.

19 Bae, S.I. and Baik, S. (1994) *J. Am. Ceram. Soc.*, **77**, 2499.

20 Krell, A. and Blank, P. (1993) *J. Am. Ceram. Soc.*, **78**, 1118.

21 Morinaga, K., Torikai, T., Nakagawa, K., and Fujino, S. (2000) *Acta Mater.*, **48**, 4735.

22 Krell, A. and Blank, P. (1996) *J. Eur. Ceram. Soc.*, **16**, 1189.

23 O, Y.T., Koo, J., Hong, K.J., Park, J.S., and Shin, D.C. (2004) *Mater. Sci. Eng.*, **A374**, 191.

24 Krell, A. and Klaffke, D. (1996) *J. Am. Ceram. Soc.*, **79**, 1139.

25 Krell, A., Blank, P., Berger, L.M., and Richter, V. (1999) *Am. Ceram. Soc. Bull.*, **77**, 65.

26 Wei, G.C. (2005) *J. Phys. D: Appl. Phys.*, **38**, 3057.

27 Krell, A., Blank, P., Ma, H., Hutzler, T., van Bruggen, M.P.B., and Apetz, R. (2003) *J. Am. Ceram. Soc.*, **86**, 12.

28 Jones, C.D., Rioux, J.B., Lochem, J.W., Bates, H.E., Zanella, S.A., Pluen, V., and Mandelartz, M. (2006) *Am. Ceram. Soc. Bull.*, **3**, 24.

29 Apetz, R. and van Bruggen, M.P.B. (2003) *J. Am. Ceram. Soc.*, **86**, 480.

30 Lim, L.C., Wong, P.M., and Jan, M.A. (2000) *Acta Mater.*, **48**, 2263.
31 Nivot, C., Valdivieso, F., and Goeuriot, P. (2006) *J. Eur. Ceram. Soc.*, **26**, 9.
32 Cheng, J., Agrawal, D., Zhang, Y., and Roy, R. (2002) *Mater. Lett.*, **56**, 587.
33 Shen, Z., Peng, H., Liu, J., and Nygren, M. (2004) *J. Eur. Ceram. Soc.*, **24**, 3447.
34 Echeberria, J., Tarazona, J., He, J.Y., Butler, T., and Castro, F. (2002) *J. Eur. Ceram. Soc.*, **22**, 1801.
35 Krell, A. and Klimke, J. (2006) *J. Am. Ceram. Soc.*, **89**, 1985.
36 Raj, R. (1981) *J. Am. Ceram. Soc.*, **64**, 245.
37 Clarke, D.R. (1987) *J. Am. Ceram. Soc.*, **70**, 15.
38 Song, H. and Coble, R.L. (1990) *J. Am. Ceram. Soc.*, **73**, 2086.
39 Bae, S.I. and Baik, S. (1993) *J. Am. Ceram. Soc.*, **76**, 1065.
40 Song, H. and Coble, R.L. (1990) *J. Am. Ceram. Soc.*, **73**, 2077.
41 Chi, M., Gu, H., Wang, X., and Wang, P. (2003) *J. Am. Ceram. Soc.*, **86**, 1953.
42 McLaren, I., Cannon, R.W., Gülgün, A.M., Voytovych, R., Popescu-Pogrion, N., Scheu, C., Täfner, U., and Rühle, M. (2003) *J. Am. Ceram. Soc.*, **86**, 650.
43 Cho, S.-J., Lee, J.-Ch., Lee, H.-L., Sim, S.-M., and Yanagisawa, M. (2003) *J. Eur. Ceram. Soc.*, **23**, 2281.
44 Lee, S.-H., Kim, D.-Y., and Hwang, N.M. (2002) *J. Eur. Ceram. Soc.*, **22**, 317.
45 Blonski, S. and Garofalini, S. (1996) *J. Phys. Chem.*, **100**, 2201.
46 Zhang, S. and Garofalini, S.H. (2005) *J. Am. Ceram. Soc.*, **88**, 202.
47 Blonski, S. and Garofalini, S.H. (1997) *J. Am. Ceram. Soc.*, **80**, 1997.
48 Zhang, S. and Garofalini, S.H. (2005) *J. Am. Ceram. Soc.*, **88** (1), 202–209.
49 Švančárek, P., Galusek, D., Loughran, F., Brown, A., Brydson, R., Atkinson, A., and Riley, F. (2006) *Acta Mater.*, **54**, 4853.
50 Cahn, R.W., Haasen, P. and Kramer, E.J. (eds) (1995) Materials Science and Technology; A Comprehensive Treatment; Chapter 2, Oxide Ceramics, in *Structure and Properties of Ceramics*, vol. 11 (vol. ed. M. Swain), VCH Weinheim, Germany, p. 99.
51 Kaysser, W.A., Sprissler, M., Handwerker, C.A., and Blendell, J.E. (1987) *J. Am. Ceram. Soc.*, **70**, 339.
52 Kim, M.-J. and Yoon, D.-Y. (2003) *J. Am. Ceram. Soc.*, **86**, 630.
53 Kim, B.-K., Hong, S.-H., Lee, S.-H., Kim, D.-Y., and Hwang, D.M. (2003) *J. Am. Ceram. Soc.*, **86**, 634.
54 Goswami, A.P., Roy, S., Mitra, M.K., and Das, G.C. (2001) *J. Am. Ceram. Soc.*, **84**, 1620.
55 Raj, R. and Lange, F.F. (1981) *Acta Metall.*, **29**, 1993.
56 Powell-Dogan, C.A. and Heuer, A.H. (1990) *J. Am. Ceram. Soc.*, **73**, 3677.
57 Powell-Dogan, C.A. and Heuer, A.H. (1990) *J. Am. Ceram. Soc.*, **73**, 3684.
58 Powell-Dogan, C.A., Heuer, A.H., Ready, M.J., and Merriam, K. (1991) *J. Am. Ceram. Soc.*, **74**, 646.
59 Wu, Y.-Q., Zhang, Y.-F., Pezzotti, G., and Guo, J.-K. (2002) *J. Eur. Ceram. Soc.*, **22**, 159.
60 Becher, P.F. (1991) *J. Am. Ceram. Soc*, **74**, 255.
61 Blendell, J.E. and Coble, R.L. (1982) *J. Am. Ceram. Soc.*, **65**, 174.
62 Zimmermann, A., Fuller, E.W. Jr, and Rödel, J. (1999) *J. Am. Ceram. Soc.*, **82**, 3155.
63 Vedula, V.R., Glass, S.J., Saylor, D.M., Rohrer, G.S., Carter, W.C., Langer, S.A., and Fuller, E.R. Jr (2001) *J. Am. Ceram. Soc.*, **84**, 2947.
64 Litton, D.A. and Garofalini, S.H. (1999) *J. Mater. Res.*, **14**, 1418.
65 Mukhopaday, A.K. and Mai, Y.-W. (1993) *Wear*, **162–164**, 258.
66 He, C., Wang, Y.S., Wallace, J.S., and Hsu, S.M. (1993) *Wear*, **162–164**, 314.
67 Rice, R.W. and Speronello, B.K. (1976) *J. Am. Ceram. Soc.*, **59**, 330.
68 Wiederhorn, S.M. and Hockey, B.J. (1983) *J. Mater. Sci.*, **18**, 766.
69 Marshall, D.B., Lawn, B.R., and Cook, R.F. (1987) *J. Am. Ceram. Soc.*, **70**, C–139.
70 Gee, M.G. and Almond, E.A. (1990) *J. Mater. Sci.*, **25**, 296.
71 Miranda-Martinez, M., Davidge, R.W., and Riley, F.L. (1994) *Wear*, **172**, 41.
72 Him, S.S., Kato, H., Hokkirigawa, K., and Abe, H. (1986) *J. Tribol.*, **108**, 522.

73 Galusek, D., Brydson, R., Twigg, P.C., Riley, F.L., Atkinson, A., and Zhang, Y.-H. (2001) *J. Am. Ceram. Soc.*, **84**, 1767.

74 Kalin, M., Jahanmir, S., and Dražič, G. (2005) *J. Am. Ceram. Soc.*, **88**, 346.

75 Insley, R.H. (1990) Electrical Properties of Alumina Ceramics, in *Alumina Chemicals: Science and Technology Handbook* (ed. L.D. Hart), The American Ceramic Society, Westerville, OH, pp. 293–297.

76 Morrell, R. (1985) in *Handbook of Properties of Technical and Engineering Ceramics, Part I, An Introduction for Engineers and Designers*, National Physical Laboratory, Her Majesty's Stationary Office, London, pp. 162–167.

77 Krupka, J., Geyer, R.G., Kuhn, M., and Hinken, J.H. (1994) *IEEE T. Microw. Theory*, **42**, 1886.

78 Matsumoto, H. (1996) Proceedings, 1996 International Accelerator School in Japan, p. 1.

79 Woode, R.A., Ivanov, E.N., Tobar, M.E., and Blair, D.G. (1994) *Electronics Lett.*, **30**, 2120.

80 Vila, R., Gonzalez, M., Mola, J., and Ibarra, A. (1998) *J. Nucl. Mater.*, **253**, 141.

81 Alford, N.M. and Penn, S.J. (1996) *J. Appl. Phys.*, **80**, 5895.

82 Itatani, K., Tsujimoto, T., and Kishimoto, A. (2006) *J. Eur. Ceram. Soc.*, **26**, 639.

83 Gardner, T.J. and Messing, G.L. (1984) *Am. Ceram. Soc. Bull.*, **63**, 1498.

84 Jost, H., Braun, M., and Carius, C. (1997) *Solid State Ionics*, **101–103**, 221.

85 Itatani, K., Kishioka, A., and Kinoshita, M. (1993) *Gypsum & Lime*, **244**, 4.

86 Misawa, T., Moriyoshi, Y., Yajima, Y., Takenouchi, S., and Ikegami, T. (1999) *J. Ceram. Soc. Jpn*, **107**, 343.

87 Smethurst, E. and Budworth, D.W. (1972) *Trans. Br. Ceram. Soc.*, **71**, 45.

88 Köbel, S., Schneider, D., Schüler, C.Chr., and Gauckler, L.J. (2004) *J. Eur. Ceram. Soc.*, **24**, 2267.

89 Itatani, K., Yasuda, R., Howell, F.S., and Kishioka, A. (1997) *J. Mater. Sci.*, **32**, 2977.

90 Ehre, D., Gutmanas, E.Y., and Chaim, R. (2005) *J. Eur. Ceram. Soc.*, **25**, 3579.

91 Chaim, R., Shen, Z., and Nygren, M. (2004) *J. Mater. Res.*, **19**, 2527.

92 Wraback, M., Shen, H., Liang, S., Gorla, C.R., and Lu, Y. (1999) *Appl. Phys. Lett.*, **74**, 507.

93 Lee, J.-M., Kim, K.-K., Park, S.-J., and Choi, W.-K. (2001) *Appl. Phys. Lett.*, **78**, 2842.

94 Pearton, S.J., Bortin, D.P., Ip, K., Heo, Y.W., and Steiner, T. (2003) *Superlattice. Microst.*, **34**, 3.

95 (1957) *Zinc Oxide Rediscovered*, The New Jersey Zinc Company, New York.

96 Shiojiri, M. and Kaito, C. (1981) *J. Cryst. Growth*, **52**, 173.

97 Tanigaki, T., Komára, S., Tamura, N., and Kaito, C. (2002) *Jpn. J. Appl. Phys.*, **41**, 5529.

98 Kutty, T.R.N. and Padmini, P. (1992) *Mater. Res. Bull.*, **27**, 945.

99 Auffredic, J.P., Boultif, A., Langford, J.I., and Louer, D. (1995) *J. Am. Ceram. Soc.*, **78**, 323.

100 Komarneni, S., Bruno, M., and Mariani, E. (2000) *Mater. Res. Bull.*, **35**, 1843.

101 Tsuchida, T. and Kitajima, S. (1990) *Chem. Lett.*, **10**, 1769.

102 Dhage, S.R., Pasricha, R., and Ravi, V. (2005) *Mater. Lett.*, **59**, 779.

103 Hwang, C.-C. and Wu, T.-Y. (2004) *Mater. Sci. Eng. B*, **111**, 197.

104 Han, J., Mantas, P., and Senos, A.M.R. (2002) *J. Eur. Ceram. Soc.*, **22**, 49.

105 Florescu, D., Mourok, L.G., Pollack, F.H., Look, D.C., Cantwell, G., and Li, X. (2002) *J. Appl. Phys.*, **91**, 890.

106 Singh, L.K. and Mohan, H. (1975) *Indian J. Pure Appl. Phys.*, **13**, 486.

107 Vojta, A. and Clarke, D.R. (1997) *J. Am. Ceram. Soc.*, **80**, 2086.

108 Matsuoka, M. (1971) *Jpn. J. Appl. Phys.*, **10**, 736.

109 Pike, G.E., Kurtz, S.R., Gourley, P.L., Philipp, H.R., and Levinson, L.M. (1985) *J. Appl. Phys.*, **57**, 5521.

110 Gupta, T.K., Straub, W.D., Ramanachalam, M.S., Schaffer, J.P., and Rohatgi, A. (1989) *J. Appl. Phys.*, **66**, 6132.

111 Ulrich, S. and Hoffmann, B. (1984) *J. Appl. Phys.*, **57**, 5372.

112 Santos, J.D., Longo, E., Leite, E.R., and Varela, J.A. (1998) *J. Mater. Res.*, **13**, 1152.

113 Clarke, D.R. (1999) *J. Am. Ceram. Soc.*, **82**, 485.

114 Metz, R., Delalu, H., Vignalou, J.R., Achard, N., and Elkhatib, M. (2000) *Mater. Chem. Phys.*, **63**, 157.

115 Caballero, A.C., Valle, F.J., and Martín Rubí, J.A. (2001) *X-Ray Spectrom.*, **30**, 273.

116 Inada, M. (1980) *Jpn. J. Appl. Phys.*, **19**, 409.

117 Olsson, E., Dunlop, G., and Oslerlund, R. (1993) *J. Am. Ceram. Soc.*, **76**, 65.

118 Mergen, A. and Lee, W.E. (1997) *J. Eur. Ceram. Soc.*, **17**, 1049.

119 Huda, D., El Baradic, M.A., Hashmi, M.S.J., and Puyane, R. (1998) *J. Mater. Sci.*, **33**, 271.

120 Bernik, S. and Daneu, N. (2001) *J. Eur. Ceram. Soc.*, **21**, 1879.

121 Mukae, K. (1987) *Am. Ceram. Soc. Bull.*, **66**, 1329.

122 Alles, A.B. and Burdick, V.L. (1991) *J. Appl. Phys.*, **70**, 6883.

123 Lee, Y.-S., Liao, K.-S., and Tseng, T.-Y. (1996) *J. Am. Ceram. Soc.*, **79**, 2379.

124 Chun, S.-Y., Shinozaki, K., and Mizutani, N. (1999) *J. Am. Ceram. Soc.*, **82**, 3065.

125 Nahm, C.-W. (2001) *J. Eur. Ceram. Soc.*, **21**, 545.

126 Nahm, C.-W., Shin, B.-C., Park, J.-A., and Yoo, D.-H. (2006) *Mater. Lett.*, **60**, 164.

127 Kuo, C.T., Chen, C.S., and Lin, I.N. (1998) *J. Am. Ceram. Soc.*, **81**, 2949.

128 Hng, H.H. and Knowles, K.M. (2000) *J. Am. Ceram. Soc.*, **83**, 2455.

129 Pfeiffer, H. and Knowles, K.M. (2004) *J. Eur. Ceram. Soc.*, **24**, 1199.

130 Saleh, H.I. and El-Meliegy, E.M. (2004) *Br. Ceram. Trans.*, **103**, 268.

131 Balzer, B., Hagemeister, M., Kocher, P., and Gauckler, L.J. (2004) *J. Am. Ceram. Soc.*, **87**, 1932.

132 Qiu, D.J., Yu, P., and Wu, H.Z. (2005) *Solid State Commun.*, **134**, 735.

133 Meagher, E.P. and Lager, G.A. (1979) *Can. Mineral.*, **17**, 77.

134 Zhang, H.Z. and Banfield, J.F. (1998) *J. Mater. Chem.*, **8**, 2073.

135 Zhang, H.Z. and Banfield, J.F. (2000) *J. Phys. Chem.*, **B104**, 3481.

136 Hwu, Y., Yao, Y.D., Cheng, N.F., Tung, C.Y., and Lin, H.M. (1997) *Nanostruct. Mater.*, **9**, 355.

137 Ye, X.S., Sha, J., Jiao, Z.K., and Zhang, L.D. (1997) *Nanostruct. Mater.*, **8**, 919.

138 Arnal, P., Corriu, R.J., Leclerq, D., Mutin, P.H., and Viox, A. (1996) *J. Mater. Chem.*, **6**, 1925.

139 Cheng, H., Ma, J., Zhao, Z., and Qi, L. (1995) *Chem. Mater.*, **7**, 663.

140 Kim, S.J., Park, S.D., and Jeong, Y.H. (1999) *J. Am. Ceram. Soc.*, **8**, 927.

141 Dhage, S.R., Pasricha, R., and Ravi, V. (2003) *Mater. Res. Bull.*, **38**, 1623.

142 Seo, D.S., Lee, J.K., and Kim, H. (2001) *J. Cryst. Growth*, **233**, 298.

143 Wilson, G.J., Will, Frost, R.L., and Montgomery, S.A. (2002) *J. Mater. Chem*, **12**, 1787.

144 Murugan, A.V., Samuel, V., and Ravi, V. (2006) *Mater. Lett.*, **60**, 479.

145 Deki, S., Aoi, Y., Hiroi, O., and Kajinami, A. (1996) *Chem. Lett.*, **6**, 433.

146 Shimizu, K., Imai, H., Hirashima, H., and Tsukuma, K. (1999) *Thin Solid Films*, **351**, 220.

147 Funakoshi, K. and Nonami, T. (2006) *J. Am. Ceram. Soc.*, **89**, 2381.

148 Wang, W., Gu, B., Liang, L., Hamilton, W.A., and Wesolowski, D.J. (2004) *J. Phys. Chem.*, **B108**, 14789.

149 Baldassari, S., Komarneni, S., Mariani, E., and Villa, C. (2005) *Mater. Res. Bull.*, **40**, 2014.

150 Pottier, A., Chaneac, C., Tronc, E., Mazerolles, L., and Jolivet, J. (2001) *J. Mater. Chem.*, **11**, 1116.

151 Kominami, H., Kohno, M., and Kera, Y. (2000) *J. Mater. Chem.*, **10**, 1151.

152 Lee, B.I., Wang, X., Bhave, R., and Hu, M. (2006) *Mater. Lett.*, **60**, 1179.

153 Templeton, A., Wang, X., Penn, S.J., Webb, S.J., Cohen, L.F., and Alford, N.McN. (2000) *J. Am. Ceram. Soc.*, **83**, 95.

154 Meng, F. (2005) *Mater. Sci. Eng.*, **B117**, 77.

155 Li, M. and Chen, Y. (1996) *Sens. Actuators*, **B32**, 83.

156 Yamada, Y., Seno, Y., Masuoka, Y., Nakamura, T., and Yamashita, K. (2000) *Sens. Actuators*, **B66**, 164.

157 Kohl, D. (1991) *Sens. Actuators*, **B1**, 158.

158 Zhang, R.-B. (2005) *Mater. Res. Bull.*, **40**, 1584.

159 Yan, M.F. and Rhodes, W.W. (1982) *Appl. Phys. Lett.*, **40**, 536.

160 Gaikwad, A.B., Navale, S.C., and Ravi, V. (2005) *Mater. Sci. Eng.*, **B123**, 50.

161 Yang, S.L. and Wu, J.M. (1993) *J. Am. Ceram. Soc.*, **76**, 145.

162 Hsiang, H.-I. and Wang, S.-S. (2006) *Mater. Sci. Eng.*, **B128**, 25.

163 Kawai, T. and Sakata, T. (1980) *Nature*, **286**, 474.

164 Hengerer, R., Kavan, L., Krtil, P., and Grätzel, M. (2000) *J. Electrochem. Soc.*, **147**, 1467.

165 SDK News Release (2005) http://www.sdk.co.jp/contents_e/news05/05-02-04.htm.

166 Liu, X., Zhao, X., Fu, R.K.Y., Ho, J.P.Y., Ding, C., and Chu, P.K. (2005) *Biomaterials*, **26**, 6143.

167 Kasuga, T., Kondo, H., and Nogami, M. (2002) *J. Cryst. Growth*, **23**, 5235.

168 Keshmiri, M. and Troczynski, T. (2003) *J. Non-Cryst. Solids*, **324**, 289.

169 Uchida, M., Kim, H.M., Kokubo, T., Fujibayashi, S., and Nakamura, T. (2003) *J. Biomed. Mater. Res.*, **64A**, 164.

170 Kurzweg, H., Heimann, R.B., Troczynski, T., and Wayman, M.L. (1998) *Biomaterials*, **19**, 1507.

171 Gulami, S.T., Helfinstine, J.D., and Davis, A.D. (1980) *J. Am. Ceram. Soc.*, **59**, 211.

172 Garvie, R.C., Urbani, C., Kennedy, D.R., and McNeuer, J.C. (1984) *J. Mater. Sci.*, **19**, 3224.

173 Garvie, R.C. (1970) Oxides of Rare Earths, Titanium, Zirconium, Hafnium, Niobium, and Tantalum, in *High Temperature Oxides, Part II* (ed. A.M. Alper), Academic Press, p. 117.

174 Heuer, A.H. and Lenz, L.K. (1982) *J. Am. Ceram. Soc.*, **65**, 192.

175 Farnworth, F., Jones, S.L., and McAlpine, I. (1980) in *Speciality Inorganic Chemicals* (ed. R. Thompson), Royal Society of Chemistry, London, p. 249.

176 Zhang, Y.L., Jin, X.J., Rong, Y.H., Hsu, T.Y., Jiang, D.Y., and Shi, J.L. (2006) *Acta Mater.*, **54**, 1289.

177 Garvie, R.C. and Goss, M.F. (1986) *J. Mater. Sci.*, **21**, 1253.

178 Garvie, R.C., Hannink, R.H., and Pascoe, R.T. (1975) *Nature*, **258**, 703.

179 Evans, A.G. and Heuer, A.H. (1981) *J. Am. Ceram. Soc.*, **63**, 241.

180 McMeeking, R.M. and Evans, A.G. (1982) *J. Am. Ceram. Soc.*, **65**, 242.

181 Ma, Y. and Kisi, E.H. (2005) *J. Am. Ceram. Soc.*, **88**, 2510.

182 Garvie, R.C., Hughes, R.R., and Pascoe, R.T. (1978) *Materials Science Research*, vol. 11 (eds H. Palmour, R.F. Davis, and T.M. Hare), Plenum Press, New York.

183 Marder, J.M., Mitchell, T.E., and Heuer, A.H. (1983) *Acta Metall.*, **31**, 387.

184 Hellman, J.R. and Stubican, V.S. (1983) *J. Am. Ceram. Soc.*, **66**, 260.

185 Hellman, J.R. and Stubican, V.S. (1983) *J. Am. Ceram. Soc.*, **66**, 265.

186 Cowley, J.D. and Lee, W.E. (1995) Materials Science and Technology; A Comprehensive Treatment; Chapter 2, Oxide Ceramics, in *Structure and Properties of Ceramics*, vol. 11 (vol. ed. M. Swain), VCH Weinheim, Germany, p. 99.

187 Tsukuma, K. and Shimada, M. (1985) *J. Mater. Sci.*, **20**, 1178.

188 Levi, C.G. (2004) *Curr. Opin. Solid State Mater. Sci.*, **8**, 77.

189 Bondioli, F., Manfredini, C.T., Ferrari, A.M., Caracoche, M.C., Rivas, P.C., and Rodriguez, A.M. (2005) *J. Am. Ceram. Soc.*, **88**, 633.

190 Rieth, P.H., Reed, J.S., and Naumann, A.W. (1976) *Am. Ceram. Soc. Bull.*, **55**, 717.

191 Gupta, T.K., Bechtold, J.H., Kuznickie, R.C., Cadoff, L.H., and Rossing, B.R. (1977) *J. Mater. Sci.*, **12**, 2421.

192 Yoshizawa, Y. and Sakuma, T. (1992) *Acta Metall. Mater.*, **40**, 2943.

193 Hwang, C.M.J. and Chen, I.W. (1990) *J. Am. Ceram. Soc.*, **73**, 1626.

194 Hendrix, W., Kuypers, S., Vangrunderbeek, J., Luyten, J., and Vandermeulen, W. (1993) *Mater. Sci. Eng. A*, **168**, 45.

195 Seidensticker, J.R. and Mayo, M.J. (1994) *Scr. Metall. Mater.*, **31**, 1749.

196 Motohashi, Y., Akutsu, S., Kakita, S., and Maruyama, Y. (2004) *Mater. Sci. Forum*, **447–448**, 305.

197 Sharif, A.A. and Mecartney, M.L. (2004) *J. Eur. Ceram. Soc.*, **24**, 2041.

198 Dillon, R.P., Sosa, S.S., and Mecartney, M.L. (2004) *Scripta Mater.*, **50**, 1441.

199 Tsurui, K. and Sakuma, T. (1996) *Scripta Mater.*, **34**, 443.

200 Chokshi, A.H. (1993) *Mater. Sci. Eng.*, **A116**, 119.

201 Jimenez-Melendo, M., Dominguez-Rodriguez, A., and Bravo-Leon, A.J. (1998) *J. Am. Ceram. Soc.*, **81**, 2761.

202 Bartolome, J.F., Montero, I., Diaz, M., Lopez-Esteban, S., Moya, J.S., Deville, S., Gremillard, L., Chevalier, J., and Fantozzi, G. (2004) *J. Am. Ceram. Soc.*, **87**, 2282.

203 Gremillard, L., Chevalier, J., Epicier, T., and Fantozzi, G. (2002) *J. Am. Ceram. Soc.*, **85**, 401.

204 Sato, T. and Shimada, M. (1986) *J. Am. Ceram. Soc.*, **68**, 356.

205 Nettleship, I. and Stevens, R. (1987) *Int. J. High. Tech. Ceram.*, **3**, 1.

206 Fang, P., Gu, H., Wang, P., Van Landuyt, J., Vleugels, J., and Van der Biest, O. (2005) *J. Am. Ceram. Soc.*, **88**, 1929.

207 Heussner, K.-H. and Claussen, N. (1989) *J. Am. Ceram. Soc.*, **72**, 1044.

208 Theunissen, G.S.A.M., Winnubst, A.J.A., and Burggraaf, A.J. (1992) *J. Eur. Ceram. Soc.*, **9**, 251.

209 Hwang, S.L. and Chen, I.-W. (1990) *J. Am. Ceram. Soc.*, **73**, 3269.

210 Xu, T., Wang, P., Fang, P., Kann, Y., Chen, L., Vleugels, J., Van der Biest, O., and Van Landuyt, J. (2005) *J. Eur. Ceram. Soc.*, **25**, 3437.

211 Reyes-Morel, P.E. and Chen, I.W. (1988) *J. Am. Ceram. Soc.*, **71**, 343.

212 Jiang, B.H., Tu, J.B., Hsu, T.Y., and Qi, X. (1992) *Mater. Res. Soc. Symp. Proc.*, **246**, 213.

213 Zhang, Y.L., Jin, X.J., Hsu, T.Y., Zhang, Y.F., and Shi, J.L. (2002) *Mater. Sci. Forum*, **394–395**, 573.

214 Claussen, N. (1976) *J. Am. Ceram. Soc.*, **59**, 49.

215 Zhu, D. and Miller, R.A. (2004) *Int. J. Appl. Ceram. Technol.*, **1**, 86.

216 Eaton, H.E. and Novak, R.C. (1987) *Surf. Coat. Technol.*, **32**, 227.

217 Zhu, D. and Miller, R.A. (2000) *J. Thermal Spray Technol.*, **9**, 175.

218 Grot, A.S. and Martyn, J.K. (1981) *Am. Ceram. Soc. Bull.*, **60**, 807.

219 Choi, S.R., Zhu, D., and Miller, R.A. (2004) *Int. J. Appl. Ceram. Technol.*, **1**, 330.

220 Gu, S., Lu, T.J., Haas, D.D., and Wadley, H.N.G. (2001) *Acta Mater.*, **49**, 2539.

221 Lu, T.J., Levi, C.G., Wadley, H.N.G., and Evans, A.G. (2001) *J. Am. Ceram. Soc.*, **84**, 2937.

222 Nicholls, J.R., Lawson, K.J., Johnstone, A., and Rickerby, D.S. (2002) *Surf. Coat. Technol.*, **383–391**, 151.

223 Clarke, D.R. and Levi, C.G. (2003) *Annu. Rev. Mater. Res.*, **33**, 383.

224 Nicholls, J.R. (2003) *Mater. Res. Soc. Bull.*, **28**, 659.

225 Harmswoth, P.D. and Stevens, R. (1992) *J. Mater. Sci.*, **24**, 611.

226 Vaßen, R., Träger, F., and Stöver, D. (2004) *Int. J. Appl. Ceram. Technol.*, **1**, 351.

227 Etsell, T.H. and Flengas, S.N. (1970) *Chem. Rev.*, **70**, 339.

228 Kharton, V.V., Naumovich, E.N., and Vecher, A.A. (1999) *J. Solid State Electr.*, **3**, 61.

229 Kharton, V.V., Marques, F.M.B., and Atkinson, A. (2004) *Solid State Ionics*, **174**, 135.

230 Inaba, H. and Tagawa, H. (1996) *Solid State Ionics*, **83**, 1.

231 Mogensen, M., Sammes, N.M., and Tompsett, G.A. (2000) *Solid State Ionics*, **129**, 63.

232 Badwal, S.P.S. (1995) *Solid State Ionics*, **76**, 67.

233 Godickemeier, M., Michel, B., Orliukas, A., Bohac, P., Sasaki, K., Gauckler, L., Heinrich, H., Schwander, P., Kostorz, G., Hofmann, H., and Frei, O. (1994) *J. Mater. Res.*, **9**, 1228.

234 Appel, C.C. and Bonanos, N. (1999) *J. Eur. Ceram. Soc.*, **19**, 847.

235 Badwal, S.P.S. and Rajendran, S. (1994) *Solid State Ionics*, **70–71**, 83.

236 Drennan, J. and Auchterlonie, G. (2000) *Solid State Ionics*, **134**, 75.

237 Lee, J.-H., Mori, T., Li, J.-G., Ikegami, T., Komatsu, M., and Haneda, H. (2000) *J. Electrochem. Soc.*, **147**, 2822.

238 Yuzaki, A. and Kishimoto, A. (1999) *Solid State Ionics*, **116**, 47.

239 Leach, C.A. (1987) *Mater. Sci. Technol.*, **3**, 321.

240 Shiratori, Y., Tietz, F., Buchkremer, H.P., and Stover, D. (2003) *Solid State Ionics*, **164**, 27.

241 Mondal, P., Klein, A., Jägermann, W., and Hahn, H. (1999) *Solid State Ionics*, **118**, 331.

242 Kosacki, I., Suzuki, T., Petrovsky, V., and Anderson, H.U. (2000) *Solid State Ionics*, **136–137**, 1225.

243 Yamamoto, O., Arachi, Y., Sakai, H., Takeda, Y., Imanishi, N., Mizutani, Y., Kawai, M., and Nakamura, Y. (1998) *Ionics*, **4**, 403.

244 Haile, M. (2003) *Acta Mater.*, **51**, 5981.

245 Weppner, W. (1992) *Solid State Ionics*, **52**, 15.

246 de Souza, S., Visco, S.J., and de Jonghe, L.C. (1997) *Solid State Ionics*, **98**, 57.

247 Murray, E.P., Tsai, T., and Barnett, S.A. (1999) *Nature*, **400**, 649.

248 Tietz, F., Fischer, W., Hauber, T., and Mariotto, G. (1997) *Solid State Ionics*, **100**, 289.

249 Hirano, M., Watanabe, S., Kato, E., Mizutani, Y., Kawai, M., and Nakamura, Y. (1998) *Solid State Ionics*, **111**, 161.

250 Hirano, M., Inagaki, M., Mizutani, Y., Nomura, K., Kawai, M., and Nakamura, Y. (2000) *Solid State Ionics*, **133**, 1.

251 Ishii, T., Iwata, T., and Tajima, Y. (1992) *Solid State Ionics*, **57**, 153.

252 Ruh, R., Garrett, H.J., Domagala, R.F., and Patel, V.A. (1977) *J. Am. Ceram. Soc.*, **60**, 399.

253 Badwal, S.P.S. (2001) *Solid State Ionics*, **143**, 39.

254 Singh, P. and Minh, N.Q. (2004) *Int. J. Appl. Ceram. Technol.*, **1**, 5.

255 Hench, L.L. (1998) *J. Am. Ceram. Soc.*, **81**, 1705.

256 Lawson, S. (1995) *J. Eur. Ceram. Soc.*, **15**, 85.

257 Chevalier, J. (2006) *Biomaterials*, **27**, 535.

258 Deville, S., Guenin, G., and Chevalier, J. (2004) *Acta Mater.*, **52**, 5697.

259 Chevalier, J., Deville, S., Münch, E., Jullian, R., and Lair, F. (2004) *Biomaterials*, **25**, 5539.

260 Munoz-Saldana, J., Balmori-Ramirez, H., Jaramillo-Vigueras, D., Iga, T., and Schneider, G.A. (2003) *J. Mater. Res.*, **18**, 2415.

261 Gremillard, L., Chevalier, J., Fantozzi, G., and Epicier, T. (2002) *J. Am. Ceram. Soc.*, **85**, 401.

262 Chi, R., Li, Z., Peng, C., Gao, H., and Xu, Z. (2006) *Metall. Mater. Trans. B*, **37B**, 155.

263 Hirano, M., Fukuda, Y., Iwata, H., Hotta, Y., and Inagaki, M. (2000) *J. Am. Ceram. Soc.*, **83**, 1287.

264 Hirano, M. and Kato, E. (1999) *J. Am. Ceram. Soc.*, **82**, 786.

265 Rossignol, S., Gerard, F., and Duprez, D. (1999) *J. Mater. Chem.*, **9**, 1615.

266 Gu, Y., Li, G., Meng, G., and Peng, D. (2000) *Mater. Res. Bull.*, **35**, 297.

267 Tsuzuki, T. and McCormick, P.G. (2001) *J. Am. Ceram. Soc.*, **84**, 1453.

268 Bai, W., Choy, K.L., Stelzer, N.H.J., and Schoonman, J. (1999) *Solid State Ionics*, **116**, 225.

269 Lee, J.-S., Lee, J.-S., and Choi, S.-C. (2005) *Mater. Lett.*, **59**, 395.

270 Mashina, S., Shaizero, O., and Meriani, S. (1992) *J. Eur. Ceram. Soc.*, **9**, 127.

271 Zhang, T.S., Ma, J., Kong, L.B., Hing, P., and Kilner, J.A. (2004) *Solid State Ionics*, **167**, 191.

272 Ishida, T., Iguchi, F., Sato, K., Hashida, T., and Yugami, H. (2005) *Solid State Ionics*, **176**, 2417.

273 Hayashi, H., Sagawa, R., Inaba, H., and Kawamura, K. (2000) *Solid State Ionics*, **131**, 281.

274 Tuller, H.L. (2000) *Solid State Ionics*, **131**, 143.

275 Kim, S. and Maier, J. (2002) *J. Electrochem. Soc.*, **149**, J73.

276 Sigmund, W.M., Bell, N.S., and Bergstrom, L. (2000) *J. Am. Ceram. Soc.*, **83**, 1557.

277 Steele, B.C.H. (2000) *Solid State Ionics*, **129**, 95.

278 Goedickemeier, M. and Gauckler, L.J. (1998) *J. Electrochem. Soc.*, **145**, 414.

279 Gerhard-Anderson, R. and Nowick, A.S. (1981) *Solid State Ionics*, **5**, 547.

280 Kilner, J.A. (1983) *Solid State Ionics*, **8**, 201.

281 Atkinson, A. and Ramos, T. (2000) *Solid State Ionics*, **129**, 259.

282 Steele, B.C.H. (2001) *J. Mater. Sci.*, **36**, 1053.

283 Inaba, H. and Tagawa, H. (1996) *Solid State Ionics*, **83**, 1.

284 Mogensen, M., Sammes, N.M., and Tompsett, G.A. (2000) *Solid State Ionics*, **129**, 63.

285 Kleinvogel, C. and Gauckler, L.J. (2000) *Solid State Ionics*, **135**, 567.

286 Zhang, T.S., Kong, L.B., Zeng, Z.Q., Huang, H.T., Hing, P., Xia, Z.T., and Kilner, J.A. (2003) *J. Solid State Electr.*, **7**, 348.

287 Zhang, T.S., Ma, J., Kong, L.B., Hing, P., Leng, Y.J., Chan, S.H., and Kilner, J.A. (2003) *J. Power Sources*, **124**, 26.

288 Lewis, G.S., Atkinson, A., Steele, B.C.H., and Drennan, J. (2002) *Solid State Ionics*, **152–153**, 567.

289 Li, J.-G., Ikegami, T., and Mori, T. (2004) *Acta Mater.*, **52**, 2221.

290 Sayle, T., Parker, S.C., and Catlow, C.R.A. (1992) *J. Chem. Soc. Chem. Commun.*, **14**, 977.

291 Logothetidis, S., Patsalas, P., and Charitidis, C. (2003) *Mater. Sci. Eng. C*, **23**, 803.

292 Lopato, L.M., Shevchenko, A.V., Kushchevskii, A.E., and Tresvyatskii, S.G. (1974) *Izv. Akad. Nauk SSSR, Neorg. Mater.*, **10**, 1481.

293 Kim, W.J., Park, J.Y., Oh, S.J., Kim, Y.S., Hong, G.W., and Kuk, I.H. (1999) *J. Mater. Sci. Lett.*, **18**, 411.

294 Sordelet, D.J. and Akinc, M. (1988) *J. Am. Ceram. Soc.*, **71**, 1148.

295 Ikegami, T., Mori, T., Yajima, Y., Takenouchi, S., Misawa, T., and Moriyoshi, Y. (1999) *J. Ceram. Soc. Jpn, Int. Ed.*, **107**, 297.

296 Sharma, P.K., Jilavi, M.H., Nab, R., and Schmidt, H. (1998) *J. Mater. Sci. Lett.*, **17**, 823.

297 Rulison, A.J. and Flagan, R.C. (1994) *J. Am. Ceram. Soc.*, **77**, 3244.

298 Subramanian, R., Shankar, P., Kavithaa, S., Ramakrishnan, S.S., Angelo, P.C., and Venkataraman, H. (2001) *Mater. Lett.*, **48**, 342.

299 Wen, L., Sun, X.D., Xiu, Z., Chen, S.W., and Tsai, C.T. (2004) *J. Eur. Ceram. Soc.*, **24**, 2681.

300 Mogilenskii, V.I. and Polonskii, A.J. (1975) *Inorg. Mater.*, **11**, 218.

301 Richardson, K. and Akinc, M. (1988) *Ceram. Int.*, **14**, 101.

302 Dutta, S.K. and Gazda, G.A. (1975) US Patent No. 3 878 280.

303 Rhodes, W.H. (1981) *J. Am. Ceram. Soc.*, **64**, 13.

304 Lefever, R.A. and Matsho, J. (1967) *Mater. Res. Bull.*, **2**, 865.

305 Reetz, T., Haase, I., Ullmann, H., and Lang, H.J. (1989) *Solid State Ionics*, **36**, 193.

306 Tsukuda, Y. and Muta, A. (1976) *J. Ceram. Soc. Jpn, Int. Ed.*, **84**, 585.

307 Yeheskel, O. and Tevet, O. (1999) *J. Am. Ceram. Soc.*, **82**, 136.

308 Desmaison-Brut, M., Montintin, J., Valin, F., and Boncoeur, M. (1995) *J. Am. Ceram. Soc.*, **78**, 716.

309 Chen, I.-W. and Wang, X.-H. (2000) *Nature*, **404**, 168.

310 Tani, T., Miyamoto, Y., Koizumi, M., and Shimada, M. (1986) *Ceramurgia Int.*, **12**, 33.

311 Fantozzi, G., Orange, G., Liang, K., and Gautier, M. (1989) *J. Am. Ceram. Soc.*, **72**, 1562.

312 Greskovich, C. and Chernoch, J.P. (1973) *J. Appl. Phys.*, **44**, 4599.

313 Harris, D.C. (1999) *Materials for Infrared Windows and Domes*, SPIE-The International Society for Optical Engineering, Washington, USA.